

# 1D YIG hole-based magnonic nanocrystal

K. O. Levchenko,<sup>1, a)</sup> K. Davidková,<sup>1,2</sup> R. O. Serha,<sup>1,2</sup> M. Moalic,<sup>3</sup> A. A. Voronov,<sup>1,2</sup> C. Dubs,<sup>4</sup> O. Surzhenko,<sup>4</sup> M. Lindner,<sup>4</sup> J. Panda,<sup>5</sup> Q. Wang,<sup>6</sup> O. Wojewoda,<sup>5</sup> B. Heinz,<sup>7</sup> M. Urbánek,<sup>5</sup> M. Krawczyk,<sup>3</sup> and A. V. Chumak<sup>1</sup>

<sup>1)</sup>Faculty of Physics, University of Vienna, Vienna, Austria

<sup>2)</sup>Vienna Doctoral School in Physics, University of Vienna, Vienna, Austria

<sup>3)</sup>Department of Physics of Nanostructures, Adam Mickiewicz University, Poznań, Poland

<sup>4)</sup>INNOVENT e. V. Technologieentwicklung, Jena, Germany

<sup>5)</sup>CEITEC BUT, Brno University of Technology, Brno, Czech Republic

<sup>6)</sup>Institute for Quantum Science and Engineering, HUST, Wuhan, China

<sup>7)</sup>Fachbereich Physik & Landesforschungszentrum OPTIMAS, RPTU, Kaiserslautern, Germany

(Dated: 16 June 2025)

Magnetic media with artificial periodic modulation—magnonic crystals (MCs) — enable tunable spin-wave dynamics and band structure engineering. Nanoscaling enhances these capabilities, making magnonic nanocrystals promising for both fundamental studies and applications. Here, we report on the design, fabrication, and characterization of one-dimensional YIG MCs with nanoholes ( $d \approx 150$  nm) spaced  $a \approx 1$   $\mu$ m apart. Micro-focused Brillouin light scattering and propagating spin-wave spectroscopy, supported by TetraX and MuMax<sup>3</sup> simulations, reveal spin-wave transmission over 5  $\mu$ m in the Damon–Eshbach configuration, and the formation of pronounced band gaps with rejection levels up to 26 dB. Detailed analysis of the spin-wave dispersion uncovered complex mode interactions, including two prominent anticrossings at 3.1 and 18.7 rad/ $\mu$ m, between which the spin-wave energy is predominantly carried by the  $n = 2$  mode, enabling efficient transmission. The results advance the development of functional MCs and open pathways toward 2D magnonic nanoarrays and magnonic RF nanodevices.

The field of magnonics explores the fundamental and applied potential of the spin waves (SW) - collective oscillations of magnetic moments in a magnetic material. The advantages offered by magnonics include high frequencies, tailored material parameters<sup>1</sup>, low energy dissipation and low power consumption, which have been successfully integrated into various prototype circuitry elements<sup>2,3</sup>, with selected concepts surpassing the performance of benchmark conventional devices<sup>4</sup>. Many of them (e.g., filters<sup>5</sup>, transistors<sup>2</sup>, sensors<sup>6,7</sup>) are realized based on magnonic crystals (MCs) - artificial magnetic materials with a spatially periodic variation of properties<sup>8–10</sup>. Growing potential of nanoscale magnonics for RF applications, including magnonic crystals, was highlighted in a recent review<sup>11</sup>. Similar to photonic crystals operating with light, MCs use the wave nature of their quasiparticles – magnons – to achieve propagation characteristics that are inaccessible by other means<sup>10,12</sup>. Key properties of MCs, such as the central frequency and band-gap width, can be tailored by adjusting (often simultaneously) by (1) the use of different materials with suitable magnetic properties (e.g., saturation magnetization<sup>13–16</sup>), (2) the choice of the periodic pattern<sup>17</sup> and (3) external factors, such as the applied magnetic field<sup>18</sup> or temperature<sup>19</sup>. Different combinations of these properties produce a variety of MC designs, including waveguide<sup>19,20</sup> – and thin-film-based<sup>12</sup> structures; one-<sup>21–25</sup>, two-<sup>26,27</sup> and three-<sup>28,29</sup> dimensional; static<sup>14,15,17</sup>, dynamic<sup>18,30</sup>, and reconfigurable<sup>19,31</sup> magnonic crystals.

The simplest and most efficient type of magnonic crystal is a one-dimensional (1D) structure with geometric patterning. Typically, a 1D MC is fabricated from a waveguide (WG), where patterning enables the structure to act as a wavevector-dependent, mode-selective system<sup>9,32</sup>. 1D MCs can function

as standalone devices or serve as building blocks for magnonic directional couplers, transistors, phase shifters, and other RF and data-processing components<sup>2</sup>. One of the fundamental works on this topic — a study on a geometrically patterned (notched) microscale permalloy 1D MC — was realized by Chumak et al.<sup>22</sup>, based on a theoretical model by Lee et al.<sup>33</sup> and numerical simulations by Ciubotaru et al.<sup>34</sup>. The authors have experimentally demonstrated the propagation of coherently excited spin waves through a metallic magnonic crystal; however, in such macrostructured waveguides, the SW dispersion is inherently multimode<sup>35</sup>, resulting in the simultaneous transmission of waves with different wavelengths at a fixed frequency. In magnonic crystals, this leads to band-gaps (BG) edges being less defined, forming a gradual slope in the transmission spectra<sup>22</sup>, rendering their operating characteristics less favorable for applications<sup>36</sup>.

To overcome this limitation, MCs based on nanowaveguides can be considered. The effects of downscaling on the spin-wave spectra were explored by Wang et al.<sup>37</sup> and by Heinz et al.<sup>38</sup> When the width of an yttrium iron garnet (YIG) waveguide is sufficiently small, exchange interaction dominates over dipolar one, leading to unpinning of SW modes. This alters the quantization condition and shifts higher-order width modes to higher frequencies, effectively providing a single-mode regime<sup>37</sup>. Nanoscale enables key advantages for applications, as shown experimentally by Davidkova et al.<sup>39</sup> in a multifunctional tunable magnonic nanodevice, or numerically by Ge et al.<sup>40</sup> in magnon nanotransistor. In the latter, notably, authors propose to use MC for precise control of the SW propagation and frequency-specific filtering. While nanoscale MCs hold great promise, their potential remains largely unrealized due to the relatively recent advances in nanofabrication.

Here, we report on experimental realization of a nanoscale 1D waveguide-based magnonic crystal, geometrically modulated with round holes. Based on our preliminary studies,

<sup>a)</sup>Electronic mail: [khrystyna.levchenko@univie.ac.at](mailto:khrystyna.levchenko@univie.ac.at)

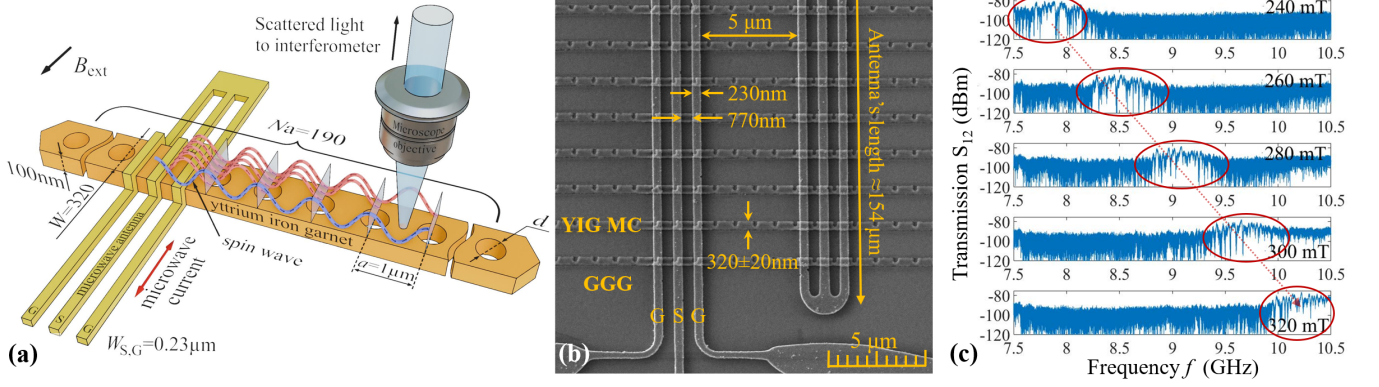


FIG. 1. (a) Sketch of 1D waveguide-based MC periodically modulated with round holes. Spin waves excited by the CPW are shown in blue, while Bragg-reflected waves - in red. Key parameters:  $w = 320$  nm – waveguide’s width;  $a = 1$   $\mu\text{m}$  – MC’s period;  $N_a \approx 200$  – total number of periods;  $d = 150$  nm – diameter of the holes; (b) SEM image of the typical 1D MC fabricated from a 100 nm-thick LPE-grown YIG/GGG film, with key parameters as in (a). The number of waveguides per antenna is  $n_{wg} = 100$ , the distance between the antennas –  $5$   $\mu\text{m}$ ; (c) Spin wave transmission signal  $S_{12}$  of magnonic crystal shown at (b) for varying bias magnetic fields in a frequency range  $7.5$  GHz -  $10.5$  GHz.

MCs with optimized geometrical parameters were designed and fabricated. Then, a detailed analysis of the spin-wave transmission in Damon-Eschbach (DE) configuration was performed with the means of Propagating Spin-Wave Spectroscopy (PSWS) across different frequency ranges, complemented by TetraX and MuMax<sup>3</sup> simulations of the dispersion relation. Finally, microfocused Brillouin Light Scattering ( $\mu$ -BLS) spectroscopy was carried out to demonstrate the spatial behavior of excitations in a single MC waveguide.

Figure 1 presents a sketch of an individual MC WG with key parameters (a) and SEM image of a section of the entire fabricated structure (b). The crystal periodicity  $a = 1$   $\mu\text{m}$  was selected to align with the maximum excitation efficiency of the antenna<sup>41</sup> (see Supplementary). The WG’s width was designed as  $w = 300$  nm to support a single SW mode in a specific range, e.g.,  $8 - 8.2$  GHz ( $< 5$  rad/ $\mu\text{m}$ ) under  $262$  mT bias field in DE and  $10.3 - 10.9$  GHz in Backward Volume configuration. After the fabrication, the width was around  $320$  nm, decreasing a single-mode window to around  $100$  MHz frequency bandwidth under same bias field. The WG’ length of  $\approx 190$   $\mu\text{m}$  was chosen to ensure that no edge-reflected SW interfere with the measurements. The hole diameter  $d$  modulates the SW reflection efficiency and thus affects the width and depth of the rejection bands<sup>10</sup>. Based on our simulations of similar structures,  $d = 150$  nm was estimated to provide the best ratio of minimized losses to well-defined BGs. The holes’ pattern persisted along the whole waveguide. All structures were realized from LPE-grown  $100$  nm-thick YIG / GGG (111) film<sup>42,43</sup> using e-beam lithography and ion etching<sup>38</sup>. To estimate the spin-wave propagation length, multiple pairs of CPW antennas with varying spacings of  $1$ ,  $2$ ,  $5$  and  $10$   $\mu\text{m}$  were fabricated. Considering the small excited magnetic volume and potentially weak PSWS signal, each separate MC structure included up to  $100$  conduits. Coplanar waveguides (CPWs) were used for coherent spin-wave excitation and detection. Fabrication parameters matched the designed ones, apart from the conduits’ width, as mentioned ear-

lier, and slight upward shift of the holes.

An exemplary propagating spin-wave spectrum, shown in Fig. 1(c), was measured on the 1D MC structure presented in Fig. 1(b). The SW transmission  $S_{12}$  was recorded while applying a fixed microwave signal with  $-10$  dBm power to the structure under test in DE configuration (in-plane,  $k \perp B_{\text{ext}}$ ). The DE geometry was selected due to its higher excitation efficiency (compared to the Backward Volume, see Supplementary materials), enabled by higher SW group velocity and stronger coupling to the in-plane antenna field. The measured complex propagating SW signal, recalculated to dB magnitude (red circles, motion direction indicated by arrow), was obtained while sweeping the magnetic field from  $240$  mT to  $320$  mT in  $20$  mT steps across  $7.5$  GHz -  $10.5$  GHz frequencies. Reference background was subtracted as shown in our earlier work<sup>39</sup>; other frequency and power ranges are provided in the Supplementary materials. The obtained SW spectrum significantly differs from that of a plain film by displaying ‘band gaps’ or ‘rejection bands’ – regions where propagation is prohibited and the signal’s magnitude drops due to the Bragg’s scattering ( $n_{mc}\lambda = 2a \cdot \sin\theta$ ,  $n_{mc}$  is an integer) of SW from the periodic holes<sup>8-10</sup>. Only the spin waves with wavenumbers  $k_a = \pm n_{mc}\pi/a$  satisfy this condition. The BG frequency depends on the material parameters, MC spatial geometry and can be tuned by the applied magnetic field, while number of gaps is defined by the Fourier distribution of spatial modulators<sup>10</sup>. Here, each hole introduces a sharp magnetic contrast (step-like function), generating multiple periodic band gaps. Accordingly, in ‘transmission’ or ‘propagation’ bands, where the Bragg condition is not satisfied, SW energy is expected to propagate without interruption, aside from higher insertion losses compared to an unstructured waveguide<sup>10</sup>. Losses at the level of  $\approx -80..-85$  dB are rather expected due to the low volume of magnetic material in structurally-modulated nanowaveguides. For reference, in a similar experiment by Davidkova et al.<sup>39</sup> on a  $97$  nm-thick unstructured YIG film, the PSWS signal displayed losses of

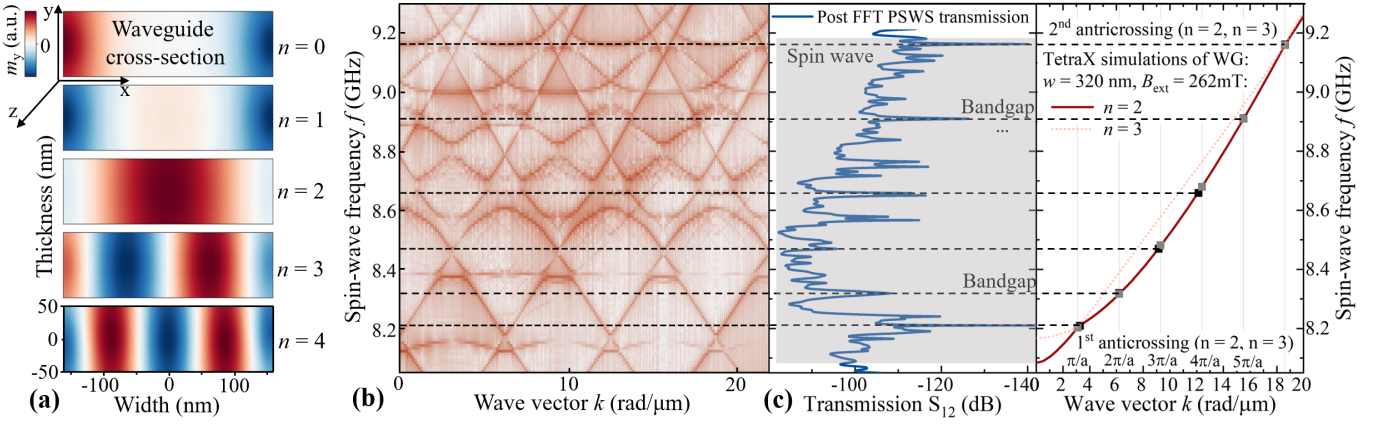


FIG. 2. (a) TetraX simulation of the mode profile amplitudes for the first 5 spin-wave modes of the unstructured waveguide in DE geometry with parameters as shown in Fig. 1(b). Real part of the magnetization dynamic component  $m_y$  is calculated for the waveguide cross-section at  $k = 0$ . (b) MuMax<sup>3</sup> micromagnetic simulation of the 1D MC dispersion relation. (c) SW transmission  $S_{12}$  at bias field  $\approx 262$  mT after 'time gating' post-analysis vs TetraX-simulated dispersion of a uniform waveguide in DE configuration. Black squares indicate the intersection of the wavenumbers  $k_a = \pm n_{mc}\pi/a$  at the band-gap frequencies with the simulated dispersion, while grey squares - with the experimental data, as indicated by the grey (c) and black (b) dashed projection lines.

$\approx -25...-35$  dB at  $-10$  dBm power level. These losses can be further reduced up to four times through optimization of antennas' SW excitation efficiency<sup>44</sup>. Therefore, having a considerable number of the conduits within one MC structure was crucial for successful signal detection, despite increasing the risk of structural imperfections affecting the transmission.

The results of TetraX<sup>45,46</sup> and Amumax<sup>47</sup> micromagnetic simulations (a fork of MuMax<sup>3</sup><sup>48,49</sup>) are presented at Fig. 2(a,c) and (b), respectively. The WG was modeled according to the geometry in Fig. 1(b) with following YIG parameters: saturation magnetization  $M_s = 139$  kA/m, exchange stiffness  $A = 3.7$  pJ/m, uniaxial magnetic anisotropy  $K_u = 3.58$  J/m<sup>3</sup> ( $\perp$  x-axis) and Gilbert damping  $\alpha = 10^{-4}$ . Bias field  $B_{ext} = 262$  mT was applied along the y-axis. Mode profiles in Fig. 2(a) were calculated for the unstructured WG cross-section at  $k = 0$ , considering only the first five ( $n = 5$ ) modes due to the quadratic decrease in dynamic magnetization intensity with increasing  $n$ . The real part of the magnetization component  $m_y$  in the DE configuration is color-coded with red and blue (more in Supplementary). The first two modes ( $n = 0, 1$ ) are edge modes, where SWs propagate only along the WG edges. Among them, only the  $n = 1$  mode could be excited due to its symmetric mode profile. However, it cannot be resolved in the experiment because of its low amplitude and group velocity. Due to lateral confinement, the profiles show only the width quantization components  $k_y = n\pi/w$ . Under direct antenna excitation, only even width modes ( $n = 2, 4, \dots$ ) are efficiently excited, as odd ones ( $n = 3, 5, \dots$ ) have no net dynamic magnetization averaged across the width. In practice, slight antenna nonuniformity can excite odd modes, albeit inefficiently. Notably, while the mode profiles appear unpinned at the top/bottom surfaces, pinning persists at the WG' edges, which introduces elastic scattering into higher-order width modes. This occurs because of the larger waveguide's width than required for complete surface pinning and single-mode operation in a wider frequency range<sup>37,38</sup>.

The dispersion relation of the MC is shown on Fig. 2(b). To obtain it, the magnetization's x-components were recorded as functions of position and time, followed by a discrete Fourier transform along both axes for each simulation cell. The absolute value of the resulting complex spectra was computed and summed over the z- and y-axes to yield the final map. Black dashed lines correspond to the intersection of the estimated resonance conditions for Bragg scattering  $k_a = \pm n_{mc}\pi/a$  with micromagnetic simulation and experimental spin-wave transmission (left panel of Fig. 2(c)). To obtain it, 'raw' data from Fig. 1(c) were subjected to 'time-gating'<sup>50</sup> post-processing (details in Supplementary materials), improving the signal-to-noise ratio and increasing BG rejection efficiency through the elimination of main spurious signals. The highest signal amplitude originates from SWs with lower wavenumbers, driven by higher group velocity and efficient CPW excitation. Exceptions occur at anticrossing points, where mode hybridization leads to spatial localization and standing wave formation, resulting in a transmission drop below 140 dB. Six distinct BGs were identified in a spectrum: five arising from the hole-induced gaps between the antennas ( $k_1 = 3.1$  rad/ $\mu$ m,  $n_{mc} = 1, \dots, 5$ ) and two anticrossings ( $k \approx 3.1$  rad/ $\mu$ m and  $k \approx 18.7$  rad/ $\mu$ m), the first coinciding with the structural gap. These anticrossings were revealed with TetraX dispersion simulation (Fig. 2(c) - right panel) for the modes  $n_{mc} = 2$  and 3 of the unstructured waveguide (crimson solid and peach dotted lines respectively). Grey squares mark intersections of the BG wavevectors  $k_a$  (thin solid gray lines) with the simulations, while black squares - with the experimental data (black dashed lines). The rejection efficiency of the band gaps is between 12.6 dB and 26.1 dB. The dispersion reveals that the investigated 1D MC operates predominantly in a single-mode within the frequencies 8.08 GHz - 8.17 GHz ( $< 3.1$  rad/ $\mu$ m). Reducing the waveguide width to approximately 280 nm is expected to eliminate mode anticrossings, while further narrowing to 250 nm would expand the single-mode

frequency range sevenfold to 7.91 GHz - 8.56 GHz (up to 12 rad/ $\mu\text{m}$ ; see Supplementary). We can also assume that within the linear regime, majority of the SW energy is effectively carried by  $n = 2$  mode in the range 8.2 GHz - 9.16 GHz (3.1 - 18.7 rad/ $\mu\text{m}$ ), since the edge modes  $n = 0, 1$  and the odd mode  $n = 3$  are not excited effectively. Both the MuMax<sup>3</sup> and TetraX simulations of an individual WG showed good agreement with the experiment, considering the cumulative PSWS signal from 100 conduits. The minor misalignment, along with the appearance of multiple weakly-defined gaps, is associated with fabrication imperfections. Variations in hole positioning and etching parameters among WGs cause reflections with slightly different amplitudes, phases, and wavelengths, leading to multiple Bragg conditions and the superposition of rejection bands.

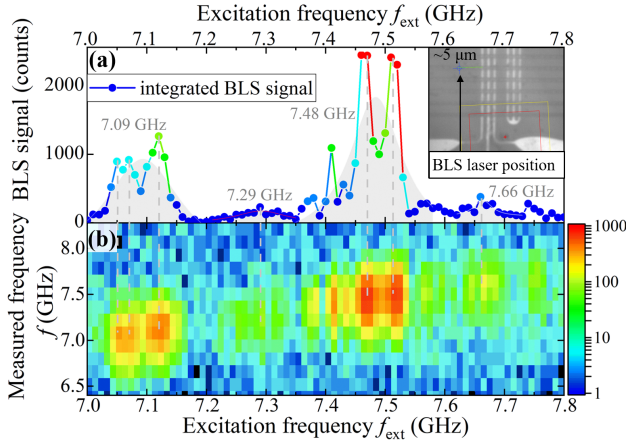


FIG. 3. BLS signal intensity of the propagating spin wave as a function of coherent excitation  $f_{\text{ext}}$  (x-axis) in a form of: (a) 2D graph, where each y-axis point corresponds to the integrated BLS counts over respective excitation frequency  $f_{\text{ext}}$ ; (b) a 3D intensity map, where the y-axis shows the full range of measured frequency  $f$  at each excitation frequency  $f_{\text{ext}}$ , and BLS signal intensity (log scale) is color-coded as z-axis. Gray-shaded areas are fitted with a Lorentzian, with the peak frequency highlighted. Measurements were performed 5  $\mu\text{m}$  away from the coplanar waveguide's antenna (inset).

After PSWS, coherently excited spin waves were probed by  $\mu$ -BLS spectroscopy<sup>51,52</sup>. An in-plane external field of  $\mu_0 H = 238.6$  mT was applied along the CPW antenna, ensuring uniform magnetization in DE configuration. Spectral analysis of the scattered light was performed using a 6-pass tandem Fabry-Pérot interferometer and a  $\lambda_{\text{Laser}} = 457$  nm<sup>53</sup> blue laser. Unlike PSWS,  $\mu$ -BLS enables probing SW propagation within a single MC nanowaveguide. Figure 3 shows the spin-wave signal, measured  $\approx 5$   $\mu\text{m}$  away from the CPW antenna (inset) on a MC with identical structural parameters to that analyzed by PSWS. Measurements were performed by sweeping the excitation frequency  $f_{\text{ext}} = 7 - 7.8$  GHz in  $\Delta f = 0.01$  GHz steps, at a constant -10 dBm power. The SW signal in the form of BLS detector intensity (counts, Stokes part) is presented as a 2D map (Fig. 3(a)), where each y-axis point corresponds to the integrated BLS counts at respective  $f_{\text{ext}}$ , and as a 3D intensity map (Fig. 3(b)), where the y-axis shows the full range of measured frequency  $f$  at each exci-

tation  $f_{\text{ext}}$ ; signal intensity color-coded as z-axis. BLS measurements were performed at the WG's center. While sweeping the microwave frequency, four periodically spaced passbands were observed (red and green areas in the 3D map), with the first signal appearing at 7.05 GHz and subsequent bands spaced by approximately 0.19 GHz. For clarity, adjacent peaks were Lorentzian-fitted (gray shaded areas), with the first peak, corresponding to the passband center, located at 7.09 GHz. Regions dominated by the background BLS counts (blue areas on the 3D map) represent five BGs measured 4.5 structural periods from the excitation antenna within a single MC waveguide. The diminishing BLS counts and the appearance of two-three separated peaks in the vicinity of 7.09 GHz and 7.48 GHz, indicate structural imperfections.

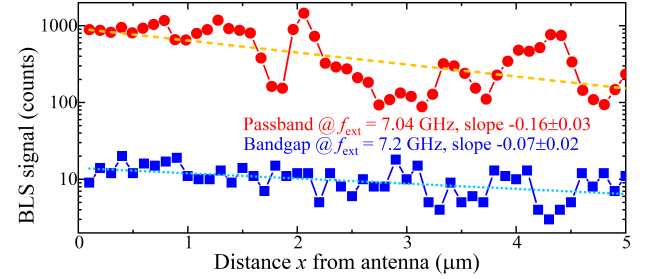


FIG. 4. BLS signal intensity of the propagating spin wave as a function of a laser scan position 0-5  $\mu\text{m}$  from the antenna (x-axis); each y-axis point corresponds to maximum BLS counts at respective passband (red) or band-gap (blue) excitation frequency.

Finally, we investigated the spin-wave transmission in the passband and band-gap regions by sweeping the laser position from 0 to 5  $\mu\text{m}$  away from the antenna in  $\approx 100$  nm step. Figure 4 demonstrates the maximum BLS intensity at the passband excitation frequency  $f_{\text{ext}} = 7.04$  GHz (red circles) and at the band-gap frequency  $f_{\text{ext}} = 7.2$  GHz (blue squares). The passband signal is an order of magnitude stronger than that of a bandgap, confirming the SW filtering. Linear fitting reveals a smaller slope for the bandgap signal (light-blue dots) compared to the passband (orange dashes), indicating suboptimal excitation efficiency and enhanced signal dissipation due to holes beneath the antenna.

In conclusion, we demonstrated efficient spin-wave propagation in nanoscale one-dimensional YIG magnonic crystal modulated with holes. PSWS and BLS investigations revealed well-defined magnonic passbands and band gaps with a rejection efficiency up to 26 dB, corresponding to Bragg scattering from the periodic holes. Single-mode operation is achieved below the first anticrossing ( $< 3.1$  rad/ $\mu\text{m}$ ) within a 100 MHz bandwidth, and can be further enhanced by narrowing the waveguides. Between the first and second anticrossings (1 GHz bandwidth, 3.1 - 18.7 rad/ $\mu\text{m}$ ), most spin-wave energy is carried by the  $n = 2$  mode, enabling effective SW transmission. While nanoscaling increases insertion losses and structural defects affecting the spectra, simulations confirm these to be only technical constraints. Future fabrication improvements are expected to firmly establish 1D YIG-based MCs as promising platforms for low-energy, high-frequency RF applications and magnonic computing.

## ACKNOWLEDGEMENTS

The research is funded by the Austrian Science Fund (FWF) project ESP 526-N TopMag [10.55776/ESP526] and by FWF IMEC [10.55776/PAT3864023]. MM and MK acknowledge Grant No. by National Science Centre of Poland (NCN) UMO–2020/37/B/ST3/03936 and 2023/49/N/ST3/03538. The work of M.L. was supported by the German Bundesministerium für Wirtschaft und Energie (BMWi) under Grant No. 49MF180119. B.H. acknowledges funding by the European Research Council within the Starting Grant No. 101042439 "CoSpiN". The authors thank Barbora Koraltan and Sabri Koraltan for the valuable discussions.

## AUTHOR CONTRIBUTIONS

K.O.L. developed and coordinated the project, performed simulations, experiments, and analysis. K.D. conducted nanofabrication and provided essential support during the preliminary design, experimental stage, and PSWS analysis. M.M. and M.K. performed key micromagnetic simulations and assisted with data interpretation. R.O.S. significantly contributed to data analysis and experiments throughout the project. A.A.V. supported with all TetraX simulations. C.D., M.L. and O.S. grew and characterized the high-quality YIG nanofilms. J.P. and M.U. provided major support during the nanofabrication process. Q.W., O.W., and B.H. assisted in establishing the BLS experiments. A.V.C. conceptualized the article framework and contributed to important scientific discussions. All authors collaboratively refined and finalized the manuscript.

## COMPETING INTERESTS

The authors declare no competing interests.

## DATA AVAILABILITY:

The data that support the findings of this study are available from the corresponding author upon reasonable request.

## REFERENCES

- 1 T. Böttcher, M. Ruhwedel, K. O. Levchenko, Q. Wang, H. L. Chumak, M. A. Popov, I. V. Zavislyak, C. Dubs, O. Surzhenko, B. Hillebrands, A. V. Chumak, and P. Pirro, *Applied Physics Letters* **120**, 102401 (2022).
- 2 A. V. Chumak, A. A. Serga, and B. Hillebrands, *Nature Communications* **5**, 4700 (2014).
- 3 G. Talmelli, T. Devolder, N. Träger, J. Förster, S. Wintz, M. Weigand, H. Stoll, M. Heyns, G. Schütz, I. P. Radu, *et al.*, *Science Advances* **6**, eabb4042 (2020).
- 4 Q. Wang, M. Kewenig, M. Schneider, R. Verba, F. Kohl, B. Heinz, M. Geilen, M. Mohseni, B. Lägel, F. Ciubotaru, *et al.*, *Nature Electronics* **3**, 765 (2020).
- 5 H. Merbouche, M. Collet, M. Evelt, V. E. Demidov, J. L. Prieto, M. Munoz, J. Ben Youssef, G. de Loubens, O. Klein, S. Xavier, *et al.*, *ACS Applied Nano Materials* **4**, 121 (2021).
- 6 M. Inoue, A. Baryshev, H. Takagi, P. B. Lim, K. Hatafuku, J. Noda, and K. Togo, *Applied Physics Letters* **98** (2011), 10.1063/1.3567940.
- 7 P. J. Metaxas, M. Sushruth, R. A. Begley, J. Ding, R. C. Woodward, I. S. Maksymov, M. Albert, W. Wang, H. Fangohr, A. O. Adeyeye, *et al.*, *Applied Physics Letters* **106** (2015), 10.1063/1.4922392.
- 8 B. Lenk, H. Ulrichs, F. Garbs, and M. Münzenberg, *Physics Reports* **507**, 107 (2011).
- 9 M. Krawczyk and D. Grundler, *Journal of Physics: Condensed Matter* **26**, 123202 (2014).
- 10 A. V. Chumak, A. A. Serga, and B. Hillebrands, *Journal of Physics D: Applied Physics* **50**, 244001 (2017).
- 11 K. O. Levchenko, K. Davidková, J. Mikkelsen, and A. V. Chumak, *arXiv* (2024), 2411.19212.
- 12 H. Puszkarski and M. Krawczyk, *Solid State Phenomena* **94**, 125 (2003).
- 13 G. Gubbiotti, S. Tacchi, M. Madami, G. Carlotti, A. Adeyeye, and M. Kostylev, *Journal of Physics D: Applied Physics* **43**, 264003 (2010).
- 14 B. Obry, P. Pirro, T. Brächer, A. V. Chumak, J. Osten, F. Ciubotaru, A. A. Serga, J. Fassbender, and B. Hillebrands, *Applied Physics Letters* **102** (2013), 10.1063/1.4807721.
- 15 M. Mruczkiewicz, P. Graczyk, P. Lupo, A. Adeyeye, G. Gubbiotti, and M. Krawczyk, *Physical Review B* **96**, 104411 (2017).
- 16 C. Dubs and O. Surzhenko, *arXiv preprint* (2025), 10.48550/arXiv.2504.03377.
- 17 Q. Wang, Z. Zhong, L. Jin, X. Tang, F. Bai, H. Zhang, and G. S. Beach, *Journal of magnetism and magnetic materials* **340**, 23 (2013).
- 18 A. Chumak, T. Neumann, A. Serga, B. Hillebrands, and M. Kostylev, *Journal of Physics D: Applied Physics* **42**, 205005 (2009).
- 19 M. Vogel, A. V. Chumak, E. H. Waller, T. Langner, V. I. Vasyuchka, B. Hillebrands, and G. Von Freymann, *Nature Physics* **11**, 487 (2015).
- 20 P. Frey, A. A. Nikitin, D. A. Bozhko, S. A. Bunyaev, G. N. Kakazei, A. B. Ustinov, B. A. Kalinikos, F. Ciubotaru, A. V. Chumak, Q. Wang, *et al.*, *Communications Physics* **3**, 17 (2020).
- 21 Y. Ikezawa, K. Nishimura, H. Uchida, and M. Inoue, *Journal of magnetism and magnetic materials* **272**, 1690 (2004).
- 22 A. V. Chumak, P. Pirro, A. A. Serga, M. Kostylev, R. Stamps, H. Schultheiss, K. Vogt, S. Hermsdoerfer, B. Laegel, P. Beck, *et al.*, *Applied Physics Letters* **95** (2009), 10.1063/1.3279138.
- 23 J. W. Klos, D. Kumar, J. Romero-Vivas, H. Fangohr, M. Franchin, M. Krawczyk, and A. Barman, *Physical Review B—Condensed Matter and Materials Physics* **86**, 184433 (2012).
- 24 H. Qin, G.-J. Both, S. J. Hämäläinen, L. Yao, and S. van Dijken, *Nature communications* **9**, 5445 (2018).
- 25 A. Roxburgh and E. Iacocca, *Magnetochemistry* **10**, 14 (2024).
- 26 S. Tacchi, M. Madami, G. Gubbiotti, G. Carlotti, A. O. Adeyeye, S. Neusser, B. Botters, and D. Grundler, *IEEE Transactions on Magnetism* **46**, 172 (2010).
- 27 S. Tacchi, P. Gruszecki, M. Madami, G. Carlotti, J. W. Klos, M. Krawczyk, A. Adeyeye, and G. Gubbiotti, *Scientific Reports* **5**, 10367 (2015).
- 28 M. Krawczyk and H. Puszkarski, *Physical Review B* **77**, 054437 (2008).
- 29 M. Krawczyk, J. Klos, M. Sokolovskyy, and S. Mamica, *Journal of Applied Physics* **108**, 093909 (2010).
- 30 A. V. Chumak, V. S. Tiberkevich, A. D. Karenowska, A. A. Serga, J. F. Gregg, A. N. Slavin, and B. Hillebrands, *Nature communications* **1**, 141 (2010).
- 31 S. Mantion, A. T. Dias, M. Madami, S. Tacchi, and N. Biziere, *J. Appl. Phys.* **135**, 053902 (2024).
- 32 A. Karenowska, A. Chumak, A. Serga, J. Gregg, and B. Hillebrands, *Applied Physics Letters* **96** (2010), 10.1063/1.3318258.
- 33 K.-S. Lee, D.-S. Han, and S.-K. Kim, *Physical review letters* **102**, 127202 (2009).
- 34 F. Ciubotaru, A. Chumak, N. Y. Grigoryeva, A. Serga, and B. Hillebrands, *Journal of Physics D: Applied Physics* **45**, 255002 (2012).
- 35 V. E. Demidov and S. O. Demokritov, *IEEE Transactions on Magnetism* **51**, 1 (2015).
- 36 Q. Wang, P. Pirro, R. Verba, A. Slavin, B. Hillebrands, and A. V. Chumak, *Science Advances* **4**, e1701517 (2018).

- <sup>37</sup>Q. Wang, B. Heinz, R. Verba, M. Kewenig, P. Pirro, M. Schneider, T. Meyer, B. Lagel, C. Dubs, T. Bracher, and A. V. Chumak, *Physical Review Letters* **122** (2019), 10.1103/PhysRevLett.122.247202.
- <sup>38</sup>B. Heinz, T. Bracher, M. Schneider, Q. Wang, B. Lagel, A. M. Friedel, D. Breitbach, S. Steinert, T. Meyer, M. Kewenig, et al., *Nano Letters* **20**, 4220 (2020).
- <sup>39</sup>K. Davıdkova, K. Levchenko, F. Bruckner, R. Verba, F. Majcen, Q. Wang, M. Lindner, C. Dubs, V. Vlaminck, J. Klıma, et al., *Physical Review Applied* **23**, 034026 (2025).
- <sup>40</sup>X. Ge, R. Verba, P. Pirro, A. V. Chumak, and Q. Wang, *Applied Physics Letters* **124**, 122413 (2024).
- <sup>41</sup>V. Vlaminck and M. Bailleul, *Physical Review B* **81**, 014425 (2010).
- <sup>42</sup>C. Dubs, O. Surzhenko, R. Linke, A. Danilewsky, U. Bruckner, and J. Del-lith, *Journal of Physics D: Applied Physics* **50**, 204005 (2017).
- <sup>43</sup>C. Dubs, O. Surzhenko, R. Thomas, J. Osten, T. Schneider, K. Lenz, J. Grenzer, R. Hubner, and E. Wendler, *Physical Review Materials* **4** (2020), 10.1103/PhysRevMaterials.4.024416.
- <sup>44</sup>F. Bruckner, K. Davıdkova, C. Abert, A. Chumak, and D. Suess, *arXiv preprint arXiv:2501.16553* (2025), 10.48550/arXiv.2501.16553.
- <sup>45</sup>L. Korber, G. Quasebarth, A. Otto, and A. Kakay, *AIP Advances* **11** (2021), 10.1063/5.0054169.
- <sup>46</sup>L. Korber, G. Quasebarth, A. Hempel, F. Zahn, A. Otto, E. Westphal, R. Hertel, and A. Kakay, Rodare (2022).
- <sup>47</sup>M. Moalic and M. Zelent, “Mathieumoalic/amumax: 2023.10.26,” (2023).
- <sup>48</sup>A. Vansteenkiste, J. Leliaert, M. Dvornik, M. Helsen, F. Garcia-Sanchez, and B. Van Waeyenberge, *AIP Adv.* **4**, 107133 (2014).
- <sup>49</sup>J. Leliaert, M. Dvornik, J. Mulkers, J. De Clercq, M. V. Milošević, and B. Van Waeyenberge, *J. Phys. D: Appl. Phys.* **51**, 123002 (2018).
- <sup>50</sup>I. Zdru, F. Ciubotaru, C. Nastase, A. Florescu, A. Abbass Hamadeh, M. Geilen, A. Nicoloiu, G. Boldeiu, D. Vasilache, S. Iordanescu, M. Nedelcu, D. Narducci, M.-C. Ciornei, C. Adelman, A. Dinescu, M. Weiler, P. Pirro, and A. Muller, *IEEE Transactions on Ultrasonics, Ferroelectrics, and Frequency Control* **72**, 30 (2025).
- <sup>51</sup>T. Sebastian, K. Schultheiss, B. Obry, B. Hillebrands, and H. Schultheiss, *Frontiers in Physics* **3**, 35 (2015).
- <sup>52</sup>O. Wojewoda, M. Hrton, and M. Urbanek, *Physical Review B* **110**, 224428 (2024).
- <sup>53</sup>B. Hillebrands, *Review of Scientific Instruments* **70**, 1589 (1999).

## “1D YIG hole-based magnonic nanocrystal” (SUPPLEMENTARY MATERIALS)

K. O. Levchenko<sup>1</sup>, K. Davidková<sup>1,2</sup>, R. O. Serha<sup>1,2</sup>, M. Moalic<sup>3</sup>, A. A. Voronov<sup>1,2</sup>, C. Dubs<sup>4</sup>, O. Surzhenko<sup>4</sup>, M. Lindner<sup>4</sup>, J. Panda<sup>5</sup>, Q. Wang<sup>6</sup>, O. Wojewoda<sup>5</sup>, B. Heinz<sup>7</sup>, M. Urbánek<sup>5</sup>, M. Krawczyk<sup>3</sup>, and A. V. Chumak<sup>1</sup>

<sup>1</sup>*Faculty of Physics, University of Vienna, Vienna, Austria*

<sup>2</sup>*Vienna Doctoral School in Physics, University of Vienna, Vienna, Austria*

<sup>3</sup>*Department of Physics of Nanostructures, Adam Mickiewicz University, Poznań, Poland*

<sup>4</sup>*INNOVENT e.V. Technologieentwicklung, Jena, Germany*

<sup>5</sup>*CEITEC BUT, Brno University of Technology, Brno, Czech Republic*

<sup>6</sup>*Institute for Quantum Science and Engineering, HUST, Wuhan, China*

<sup>7</sup>*Fachbereich Physik & Landesforschungszentrum OPTIMAS, RPTU, Kaiserslautern, Germany*

### 1. Fabrication recipe

Considering the progress in material science and nanostructuring, the topic of magnonic crystals is making a swift comeback onto researchers' radar with, e.g., recently published works by Merbouche et al. [S1], on frequency filtering using width-modulated nanoscale Yttrium Iron Garnet (YIG) magnonic crystals (MCs), and by Manton et al., who demonstrated reconfigurable spin-wave modes in a Heusler magnonic nanocrystal [S2]. Yet, the process of nanostructuring is complex and remains largely empirical, with no universal fabrication protocol. Currently, the limits of fabrication techniques define the minimum lateral size, which for us is around 50–100 nm for 100 nm-thick YIG films, increasing to around 300 nm for more complex periodic structures to guarantee repeatability and reliability.

To achieve the desired parameters of a 300 nm-wide MC waveguide periodically modulated with 150 nm-diameter holes along the entire conduit and considering 10 – 100 of such parallel waveguides on coplanar waveguide (CPW) antennas, our recipe included four main parts: fabrication of alignment markers, ‘windows’ at the position of the waveguides (using chromium as the hard mask, ‘positive procedure’), fabrication of magnonic crystals (using CSAR as a hard mask, ‘negative procedure’), and excitation antennas. Each part follows a similar set of steps: 1) cleaning and spin-coating (adhesion layer + resist CSAR for MC, PMMA – for rest + conductive layer ELECTRA); 2) electron beam writing of the target design (30 kV, 100 pA for MC and antennas, 9.23 nA for pads, labels, ‘waveguides windows’); 3) developing (AR 600-546 for MC, AR 600-56 for the rest); 4) ion beam etching for MC or PMMA etch + evaporation + lift-off – for markers and antennas. After etching, the residual chromium mask was dissolved with Cr solvent. Microwave antennas were fabricated on top of MC conduits using e-beam lithography and electron-beam physical vapor deposition (10 nm Ti, 320 nm Cu, 20 nm Au).

To ensure optimal sampling control, each structure contains only one varying parameter, associated either with the magnonic crystal or distance between the antennas, and was replicated at different chip locations to minimize the impact of potential fabrication defects. The length of the waveguide was set to approximately 190  $\mu\text{m}$ , based on preliminary estimation of the spin-wave propagation length in YIG thin films, ensuring that reflected spin waves from the waveguide edges do not interfere with the measurements. An alternative approach would be to use shorter waveguides while coating their ends with a thin gold layer to suppress backscattered signals [S3].

### 2. Antenna's excitation efficiency and dispersion relation calculation

In order to excite and detect spin waves in one-dimensional (1D) YIG MC periodically modulated with holes, each structure contained a pair of CPW antennas, spaced 1, 2, 5 and 10  $\mu\text{m}$  apart. The antenna dimensions were optimized to maximize excitation efficiency and accessible wavenumber range, while also enabling the detection of multiple band gaps. Additionally, the design ensures operation at moderate microwave power levels, characteristic impedance  $z_0 \approx 77 \Omega$  for the excitation region and  $z_0 \approx 50 \Omega$  for the contact pads. Our previous experience with nanoscale YIG structures has shown that a reliable CPW antenna configuration has a ground-signal-ground (G-S-G) line layout, where the widths of the signal (S) and ground (G) lines are approximately 230 nm, and the gap between them is about 770 nm in the excitation region. The excitation efficiency of the CPW antenna is calculated based on the model proposed by Vlaminck et al., [S4], following the formula:

$$J_{\text{exc}} = \left| \frac{2 \cdot \sin\left(\frac{k_t \cdot l_g}{2}\right)}{k_t \cdot l_g} + \frac{\sin\left(k_t \cdot \left(\frac{l_g}{2} + l_1\right)\right) - \sin\left(k_t \cdot \left(\frac{l_g}{2} + l_1 + l_p\right)\right)}{k_t \cdot l_p} \right|^2$$

where  $l_g$  – width of a CPW signal line;  $l_p$  – width of a CPW ground line;  $l_1$  – distance between a signal and a ground line;  $k_t$  – wavevector.

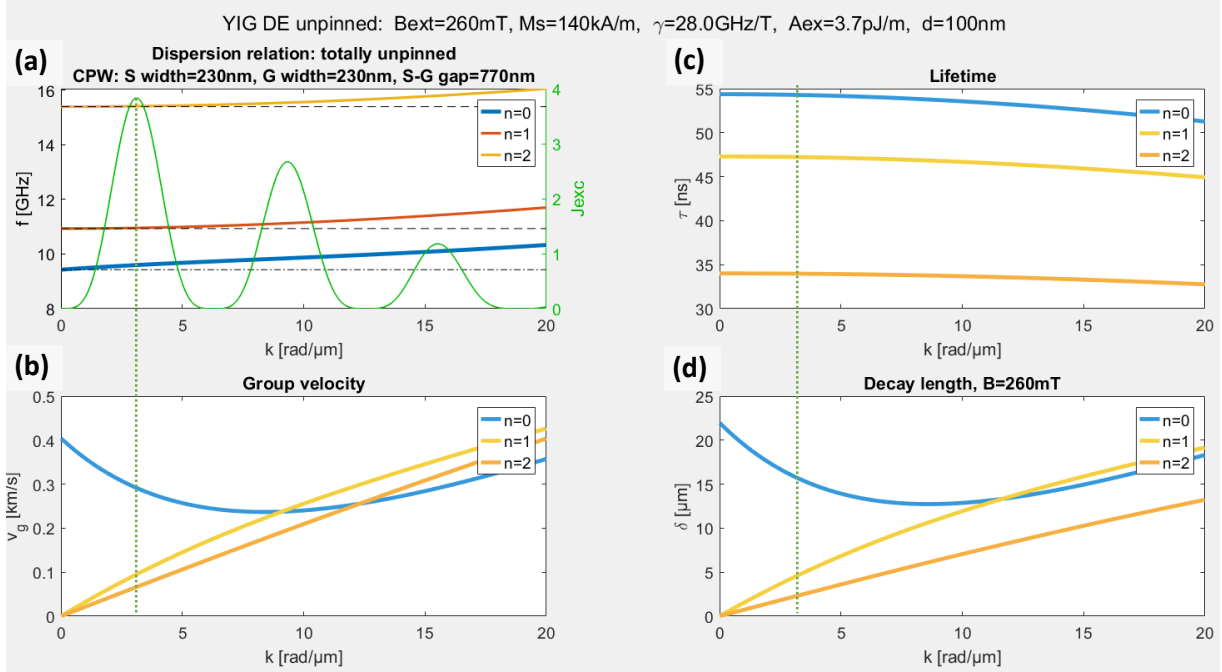


**Fig. S1:** Analytical calculation of the first three modes in 100 nm-thick YIG unstructured film ( $M_s = 176$  mT,  $\gamma = 28$  GHz/T,  $A_{\text{ex}} = 3.7$  pJ/m) in Damon-Eshbach configuration under  $\mu_0 H_{\text{ext}} = 260$  mT bias field: **(a)** dispersion relation and CPW antenna's (ground-signal-ground, G-S-G,  $w_{\text{S,G}} \approx 230$  nm,  $w_{\text{S-G}} \approx 770$  nm) excitation efficiency  $J_{\text{exc}}$ ; **(b)** group velocity  $v_g$  (km/s); **(c)** lifetime  $\tau$  (ns); **(d)** decay length  $\delta$  ( $\mu\text{m}$ ). Green dotted line represents a projection of a wavevector  $k \approx 3.1 \frac{\text{rad}}{\mu\text{m}}$  corresponding to the lattice period of 1  $\mu\text{m}$ .

The results of the analytical calculation of the dispersion relation for the first three spin-wave modes in an unstructured 100-nm-thick YIG film, together with the excitation efficiency  $J_{\text{exc}}$  of the CPW antenna, are presented in Fig. S1(a). We have considered standard magnetic parameter of the YIG film:  $M_s = 176$  mT,  $\gamma = 28$  GHz/T,  $A_{\text{ex}} = 3.7$  pJ/m, Damon-Eshbach (DE) configuration under the 260 mT bias magnetic field. In addition, we have also estimated the group velocity –  $v_g$  (Fig. S1(b)), lifetime  $\tau$  (Fig. S1(c)), decay length  $\delta$  (Fig. S1(d)). According to Kalinikos and Slavin [S5, S6], the analytical description of the dipole-exchange spin waves in a ferromagnetic film considering the spin pinning condition is:

$$f = \frac{\gamma}{2\pi} \sqrt{\left(B_{\text{ext}} + \frac{2A_{\text{ex}}}{M_s} k^2\right) \left(B_{\text{ext}} + \frac{2A_{\text{ex}}}{M_s} k^2 + \mu_0 M_s F_n\right)},$$

where  $k$  – total wavevector,  $k = \sqrt{k_t^2 + k_n^2}$ ;  $k_t$  – tangential wavevector, which corresponds to the spin-wave propagation in the magnetic film;  $k_n = \frac{n\pi}{d}$  – perpendicular wavevector, which is quantized and defined by the film thickness  $d$ ;  $\mu_0$  – vacuum permeability;  $\gamma$  – gyromagnetic ratio;  $A_{\text{ex}}$  – exchange stiffness;  $M_s$  – saturation magnetization;  $B_{\text{ext}}$  – external magnetic field;  $F_n$  – angular and boundary-condition-dependent term:

$$F_n = \sin^2 \theta + P_n \left[ \cos(2\theta) + \sin^2 \theta \cdot \sin^2 \phi \cdot \left( 1 + \frac{\mu_0 M_s (1 - P_n)}{B_{\text{ext}} + \frac{2A_{\text{ex}}}{M_s} k^2} \right) \right],$$

where  $\theta$  is an azimuthal angle,  $\theta = \pi/2$  indicates in-plane magnetization;  $\phi$  is the in-plane polar angle between the direction of spin-wave propagation and the direction of an effective field,  $\phi = \pi/2$  corresponds

to wavevector perpendicular to magnetization,  $P_n$  – spin-pinning condition term, which for unpinned magnetic moments is defined as:

$$P_n = \frac{k_t^2}{k^2} \left[ 1 - \frac{2k_t(1-(-1)^n e^{-k_t d})}{dk^2(1+\delta)} \right] \text{ with Kronecker's delta } \delta = \begin{cases} 1, & n = 0 \\ 0, & n \neq 0 \end{cases}.$$

Group velocity  $v_g$  was evaluated as a derivative of the dispersion relation:

$$v_g(k_t) = \frac{d\omega}{dk} = 2\pi \cdot \frac{df_n}{dk} \approx 0.291 \text{ (km/s)},$$

where  $f_n$  – frequency dispersions for the respective quantization number  $n = 0, 1, 2, \dots$ ;  $\omega = 2\pi f$  – angular frequency.

Lifetime was calculated as a field derivative of the dispersion relation:

$$\tau = \left( \alpha \omega \frac{d\omega}{d\omega_H} \right) \approx 54 \text{ (ns)},$$

where  $\alpha$  – Gilbert damping constant.

Decay length was calculated according to:

$$\delta = v_g \cdot \tau \approx 15.8 \text{ (}\mu\text{m)}.$$

Maximum excitation efficiency of the planned CPW antenna corresponds to  $k \approx 3.1 \frac{\text{rad}}{\mu\text{m}} \rightarrow \lambda \approx 2 \mu\text{m}$ .

The Bragg scattering condition of a 1D MC in the form of a periodic array of reflecting planes (holes) is defined as  $n_{mc}\lambda = 2a \sin\theta_{mc}$ , where  $n_{mc}$  is integer,  $\lambda$  – spin-wave wavelength,  $a$  – lattice constant (magnonic crystal period),  $\theta_{mc}$  – incident spin-wave angle. Assuming normal incidence ( $\theta_{mc} = \pi/2$ ), we set the MC period to  $a = 1 \mu\text{m}$  to achieve optimal excitation.

### 3. Micromagnetic simulations

#### 3.1 TetraX mode profiles

TetraX micromagnetic simulations were performed for the mode profiles in the DE and Backward Volume (BV) magnetization configuration of an unstructured waveguide cross-section considering (Fig. S2):  $M_s = 174.7 \text{ mT}$ , uniaxial magnetic anisotropy  $K_u = 3.58 \text{ J/m}^3$  ( $\perp$  x-axis); Gilbert damping  $\alpha = 10^{-4}$ ; waveguide's thickness  $d = 100 \text{ nm}$ ; waveguide's width  $w = 320 \text{ nm}$ . Profiles were calculated for  $k = 0$ , considering only the first five ( $n = 5$ ) modes due to the quadratic decrease in dynamic magnetization intensity with increasing  $n$ . The real part of the respective magnetization components –  $m_y$  for DE,  $m_x$  for BV – is color-coded with red and blue.

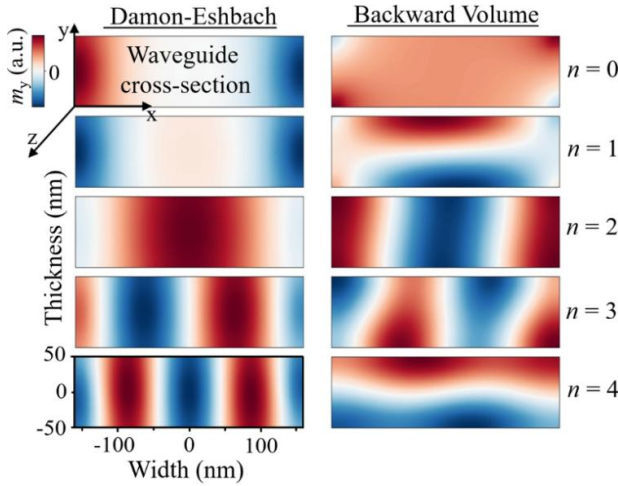


**Fig. S2:** TetraX simulation of the mode profile amplitudes for the first 5 spin-wave modes of the unstructured waveguide in DE and BV geometry.

Profiles exhibit both width and thickness quantization due to lateral confinement. In the DE configuration, all modes show only width quantization, with components  $k_y = n\pi/w$ , whereas the BV configuration displays a more complex mix of thickness and width contributions, evident from the horizontal and diagonal color patterns. The DE modes with  $n = 0, 1$  are edge modes, where spin waves propagate only along the waveguide edges. Slight non-uniformities in the BV profiles, such as in the  $n = 0$  mode, arises from plotting a single magnetization component, while contributions from both dynamic components  $m_y$  and  $m_x$  are

important. Although the mode profiles are unpinned at the top and bottom surfaces, edge pinning persists, introducing elastic scattering into higher-order width modes. This effect occurs because the waveguide width slightly exceeds the critical threshold required for complete unpinning and single-mode operation. The impact of edge pinning is more pronounced in DE modes due to their intrinsically nonreciprocal and edge-localized nature, which leads to mode anticrossing at lower wavevectors. Nevertheless, simulations confirm that for the selected MC waveguide geometry, the DE configuration provides the clearest understanding and control of spin-wave transmission.

### 3.2. MuMax<sup>3</sup> dispersion relation of the 1D magnonic crystal waveguide

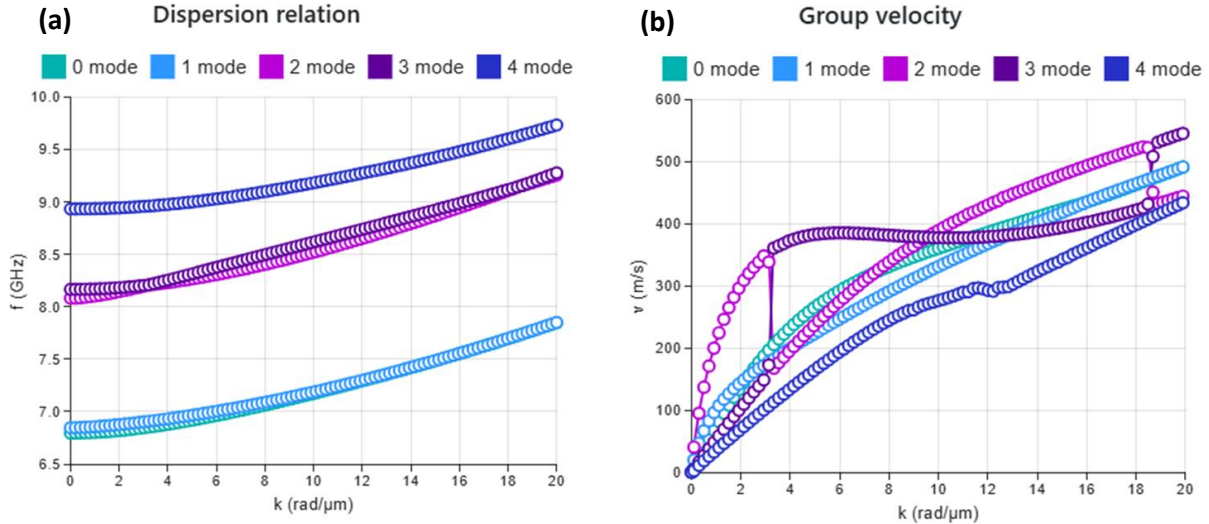
The dispersion relation of the MC structure shown in Fig. 2(b) of the main article was calculated using Amumax, a fork of MuMax<sup>3</sup>. The simulated geometry had parameters equal to those of the fabricated structures. The computational domain was discretized into  $215 \times 25 \times 1$  cells, corresponding to a spatial resolution of  $6.1 \times 10 \times 100$  nm along the x-, y-, and z-axes, respectively. The waveguide was modeled using YIG material parameters, with a saturation magnetization  $M_s = 174.7$  mT, exchange stiffness  $A_{\text{ex}} = 3.7 \cdot 10^{-12}$  J/m, and uniaxial magnetic anisotropy  $K_u = 3.58$  J/m<sup>3</sup>, oriented perpendicular to the x-axis. The Gilbert damping constant was set to  $\alpha = 10^{-4}$ . A static bias field of  $B_{\text{ext}} = 260$  mT was applied along the y-axis. To break any residual symmetry that could lead to nonphysical results, additional static fields of 1 mT were applied along the x- and z-axes. Absorbing boundary conditions were implemented by gradually increasing the damping parameter near the edges of the waveguide.

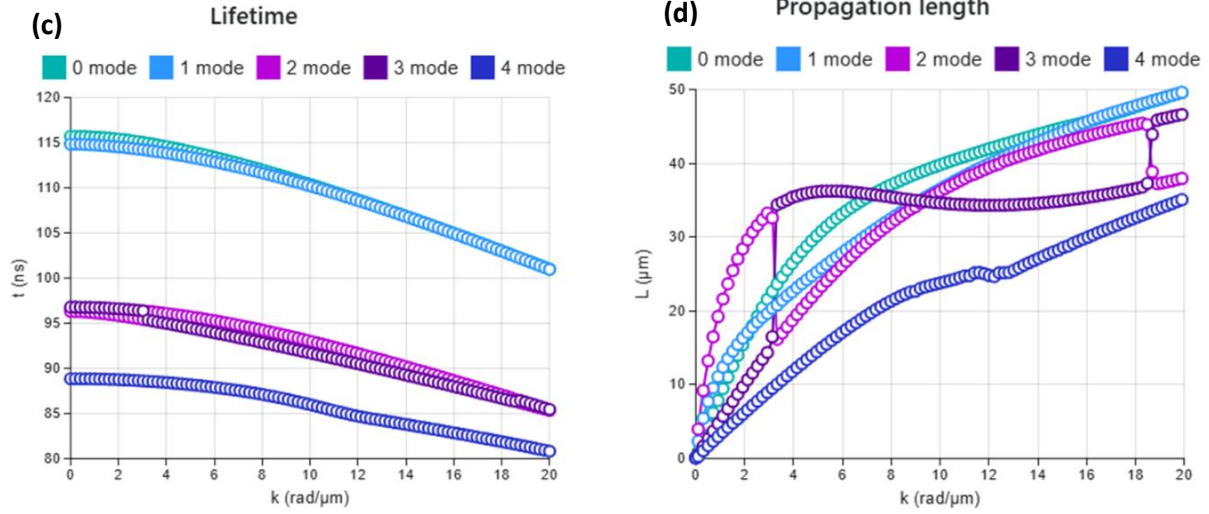
The simulation proceeded in two stages. First, the system was relaxed to its magnetic ground state. Subsequently, spin waves were excited using a sinc-shaped magnetic field applied spatially, ensuring uniform excitation of wavevectors below  $10^0 \times 10^6$  rad/m. The temporal profile of the excitation field also followed a sinc function, with a cut-off frequency of 15 GHz and a peak amplitude of  $5 \times 10^{-4}$  T. The excitation was applied over a duration of 100 ns, and the x-component of the magnetization was sampled every 25.6 ps during this period. To compute the dispersion relation, the x-components of the magnetization were recorded as functions of time and position. A discrete Fourier transform was applied along both the time and x-axes using the fast Fourier transform (FFT) algorithm for each simulation cell. The absolute value of the resulting complex spectra was computed and summed over the z- and y-axes to yield the final dispersion map.

The spin-wave dispersion enabled the estimation of the relative positions of the band gaps within the magnonic spectrum and was in good agreement with TetraX dispersion calculation.

### 3.3. TetraX simulations

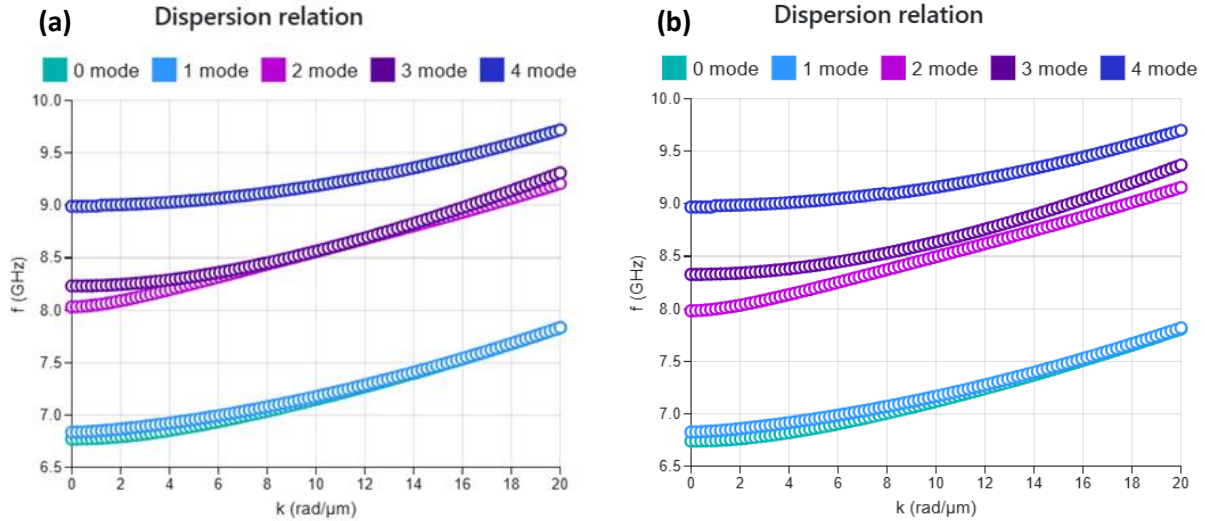
The dispersion relation as a function of the microwave frequency (Fig. 2(c) of the main article) was analytically calculated for a single unstructured MC conduit to match the experimental data. The calculations were performed using an open-source TetraX-based software, developed within the Nanomagnetism and Magnonics group by A. A. Voronov et al., at the University of Vienna (<https://www.madivie.at/>). Common input parameters for all calculated structures were: Damon-Eschbach configuration,  $B_{\text{ext}} = 262$  mT; waveguide of width  $w = 320$  nm,  $t = 100$  nm;  $M_s = 174.7$  mT; in-plane anisotropy  $K_u = 3.58$  J/m<sup>3</sup>; exchange constant  $A_{\text{ex}} = 3.7 \cdot 10^{-12}$  J/m; Gilbert damping  $\alpha = 2 \cdot 10^{-4}$ ; wavevector range  $k = 0 \dots 20$  rad/ $\mu\text{m}$ ; number of  $k$ -values = 100; mash cell size  $dx, dy = 5$ , number of modes  $n = 5$ .





**Fig. S3:** TetraX micromagnetic simulation of the unstructured waveguide with a width  $w = 320$  nm, thickness  $t = 100$  nm, saturation magnetization  $M_s = 174.7$  mT, and external magnetic field  $\mu_0 H_{\text{ext}} = 262$  mT for the  $n = 5$  modes: (a) spin-wave dispersion relation; (b) group velocity; (c) lifetime; (d) propagation length.

Notably, in the main article, only the modes  $n = 2$  and 3 of the unstructured waveguide are shown with crimson solid and peach dotted lines respectively. In the Supplementary (Fig. S3), all 5 modes are shown in colors according to the program's default palette, with modes 2 and 3 represented with purple and plum circles, as noted in the figures' legend. First two modes correspond to the edge states, while the lowest fundamental width mode is  $n = 2$ . The derived parameters for the second mode around  $k \approx 3.1$   $\text{rad}/\mu\text{m}$  are estimated as: group velocity  $v_g \approx 340$  m/s (Fig. S3(b)), lifetime  $\tau \approx 95.9$  ns (Fig. S3(c)), propagation length  $l \approx 32.7$   $\mu\text{m}$  (Fig. S3(d)). At the  $k \approx 3.1$   $\text{rad}/\mu\text{m}$  and  $18.7$   $\text{rad}/\mu\text{m}$  spin waves modes  $n = 2$  and  $n = 3$  are hybridized, forming anticrossing points, where energy is exchanged between the modes.



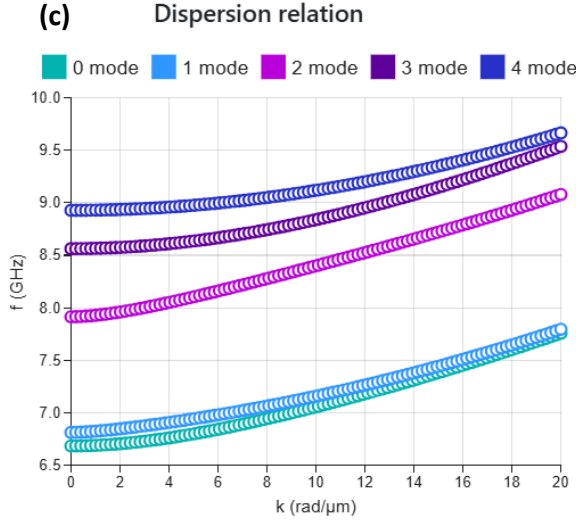


**Fig. S4:** TetraX micromagnetic simulations of the dispersion relations of an unstructured waveguide with parameters as in Fig. S3, varying in width: (a) width  $w = 300$  nm; (b) width  $w = 280$  nm; (c) width  $w = 250$  nm.

Comparing Fig. S1 to Fig. S3 it is clearly visible how the much the dispersion relation of a thin film differs from the unstructured nanowaveguide. Firstly, a magnon frequency decreases in a waveguide under similar external magnetic field is primarily due to demagnetization field and mode confinement, which alters the effective internal field and dispersion relation. For discussed waveguide's configuration, mode localization ( $n = 2, 3$ ) leads to two anticrossing points – at  $k \approx 3.1$  rad/μm and  $k \approx 18.7$  rad/μm. Therefore, a single-mode is expected within the frequency bandwidth of 100 MHz ( $f \sim 8.08 - 8.17$  GHz,  $k < 3.1$  rad/μm). Secondly, tuning of the geometrical parameters of the conduit, primary its width, most prominently affects the shape of the dispersion and modes hybridization.

For example, Fig. S4(a) shows the TetraX simulations of the dispersion relation for the waveguide with the same input parameters apart from the width set to originally designed 300 nm, while Fig. S4(b) and (c) – width set to 280 nm and 250 nm, respectively. It is clearly visible how the decrease of the width to 300 nm leads to the appearance of only 1 anticrossing point at  $k \approx 8.11$  rad/μm, increasing the single-mode bandwidth to 200 MHz (8.03 – 8.23 GHz). Reducing the waveguide width to approximately 280 nm eliminates mode anticrossings, while further narrowing to 250 nm expands the single-mode frequency range sevenfold to 7.91 – 8.56 GHz (up to 12 rad/μm). A wider single-mode frequency bandwidth for the original structure is accessible in Backward Volume configuration – from 10.27 GHz to 10.94 GHz for the same input parameters (see Fig. S5). However, the excitation efficiency in such configuration was too low for measurement consideration.

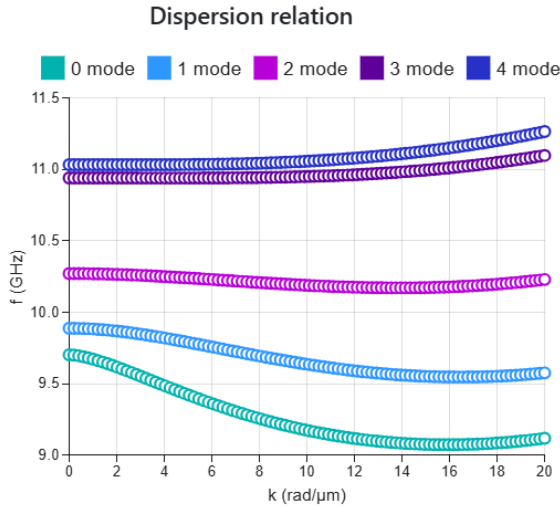


**Fig. S5:** TetraX micromagnetic simulation of the dispersion relation for an unstructured waveguide with the same parameters as in Fig. S3, but in the Backward Volume geometry.

#### 4. Propagating spin-wave spectroscopy experimental set-up

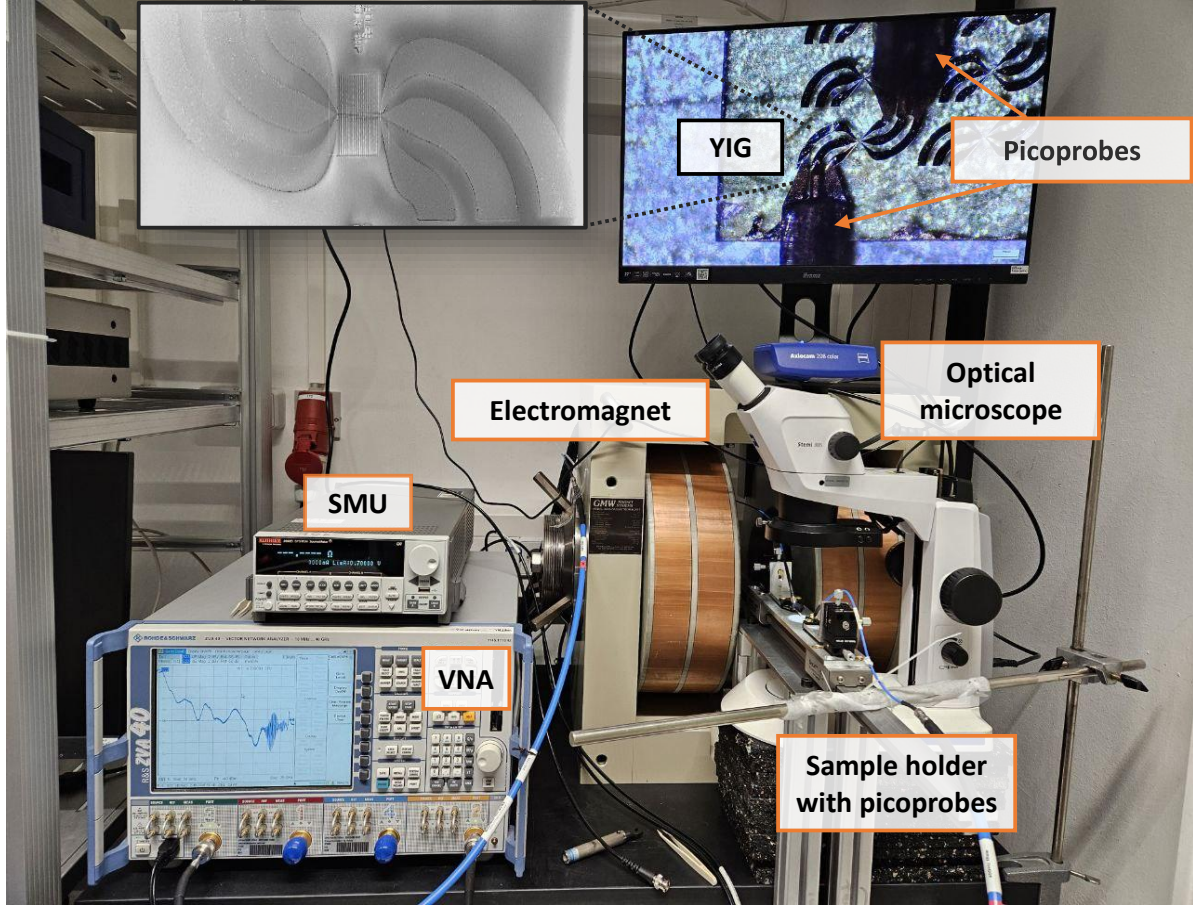


**Fig. S6:** Experimental setup used in propagating spin-wave spectroscopy (PSWS) measurements, consisting of key equipment: Vector Network Analyzer (VNA), coaxial k-type cables and adapters, 40A-GSG-150-P picoprobes, GMW 3473-70 electromagnet, Source Measurement Unit (SMU) and optical microscope.

All-electrical propagating spin-wave spectroscopy (PSWS) measurements were carried in the set-up shown in Fig. S6. The set-up consists of a Vector Network Analyzer, VNA (4-port Rhode & Schwarz ZVA-40) connected to an H-frame electromagnet GMW 3473-70 with a tunable air gap for various measurement configurations and magnet poles of 15 cm diameter to induce a sufficiently uniform biasing magnetic field ( $\mu_0 H_{\text{ext}} = <0.6 \dots 2.1$  T depending on the air gap). The calibrated VNA signal was transferred via k-type cables/non-magnetic adapters to a pair of 40A-GSG-150-P picoprobes connected to the contact pads of the fabricated CPW antennas. All the measurements were performed at  $T_{\text{RT}} \approx 295$  K. To avoid non-linear contributions from multimagnon scattering processes, preserve the antennas during extended measurements, yet achieve an optimal signal efficiency, we kept the RF power at -10 dBm. Sample is located between the picoprobes on a sample holder, and can be rotated with respect to the required magnetization geometry.

After applying sufficient magnetic field to homogenously magnetize the sample, VNA-generated high-frequency signal is transferred to a CPW antenna fabricated on top of the structure of interest. The applied microwave signal induces an alternating Oersted magnetic field around the antenna. Its components perpendicular to the bias field provide the necessary torque to excite precessional motion of spins in the magnetic medium directly under the antenna. If the correct conditions for the bias magnetic field and frequency are satisfied, this excitation launches propagating spin waves. By symmetry, the spin-wave detection mechanism through the output antenna is the inverse of the excitation. The VNA measures the transmitted and reflected signals, enabling the extraction of key parameters of transmission spectra, such as insertion loss, electromagnetic leakage, attenuation level, etc. VNA parameters used for the measurements were an intermediate frequency bandwidth 0.1-1 kHz, a frequency step 100 kHz and no averaging. Proper connection of picoprobes to sample's contact pads and evaluation of antennas' resistance was done via the Source Measurement Unit (SMU).

## 5. PSWS – different frequency ranges and ‘time gating’ for signal-to-noise improvement

Propagating spin-wave spectroscopy transmission signal  $S_{12}$  of 100 nm-thick 1D YIG hole-based MC is shown on Fig. S7. The structure under study is same as demonstrated at Fig.1(c) of the main article and was measured under same conditions (Damon-Eshbach configuration; microwave signal power level set to -10 dBm). The reference background signal, taken at magnetic fields slightly below the excitation level, was subtracted to improve the signal-to-noise ratio. Most clear signal is demonstrated at Fig. S7(b) due to the optimal combination of the preliminary designed antenna’s excitation efficiency and high spin-wave group velocity.

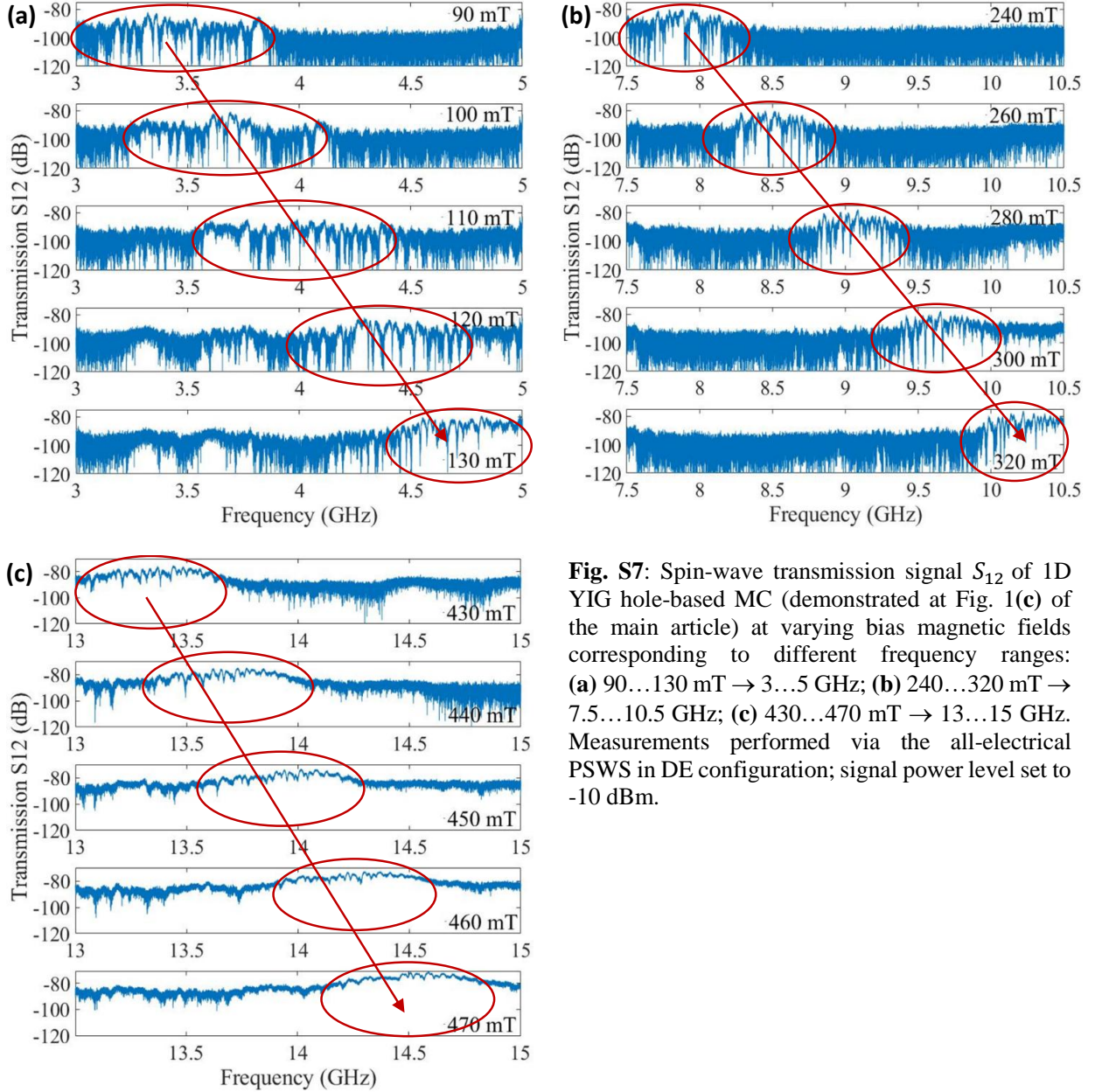


**Fig. S7:** Spin-wave transmission signal  $S_{12}$  of 1D YIG hole-based MC (demonstrated at Fig. 1(c) of the main article) at varying bias magnetic fields corresponding to different frequency ranges: (a) 90...130 mT  $\rightarrow$  3...5 GHz; (b) 240...320 mT  $\rightarrow$  7.5...10.5 GHz; (c) 430...470 mT  $\rightarrow$  13...15 GHz. Measurements performed via the all-electrical PSWS in DE configuration; signal power level set to -10 dBm.

To further improve the signal-to-noise ratio and subtract the electromagnetic leakage, we have used ‘time gating technique’, widely applied in Surface Acoustic Waves (SAW) analysis [S7, S8]. Firstly, the real and imaginary parts of the quasi-continuous  $S_{12}$  VNA signal and its reference were respectively subtracted from each other before being subjected to Inverse FFT (IFFT) – Fig. S8(a). A significant source of a signal disruption originates from electromagnetic leakage generated by the antenna itself, which propagates between the CPW antennas at a speed of light within a first nanosecond (up to 2 ns considering reflection-induced smearing), and is identified in the time domain as a first pulse of strong amplitude. The SW signal is expected to have a propagation time of around 14.7 ns, considering the  $\approx 5 \mu\text{m}$  distance between the antennas and the

spin-wave velocity of  $\approx 340$  m/s (according to the TetraX simulations of the unstructured waveguide, *Section 3.3* of the Supplementary materials for the lowest fundamental volume mode  $n = 2$  slightly below  $3.1$  rad/ $\mu\text{m}$ ). This closely matches the second pulse found in the time-domain data, appearing at  $13.6$  ns. Therefore, a SW transmission window is further fixed to the time frame  $13.6$  ns –  $90$  ns, while setting the rest to zero, to eliminate the parasitic signal and noise. The obtained signal is then transformed back to the frequency domain via the FFT – Fig. S8(b). Note, that we do not differentiate here between the pure SW transmission and reflected components, e.g., triple transit.

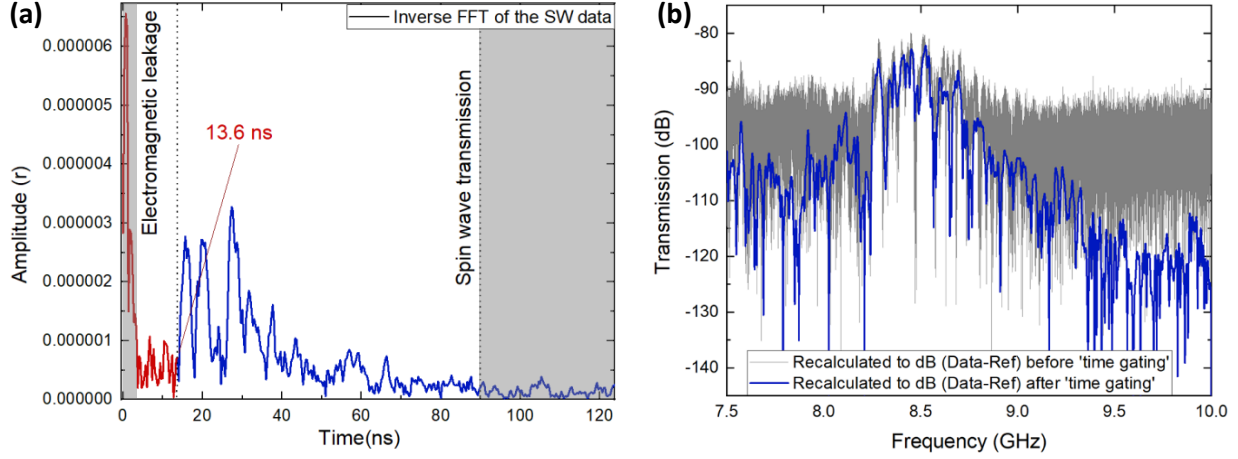
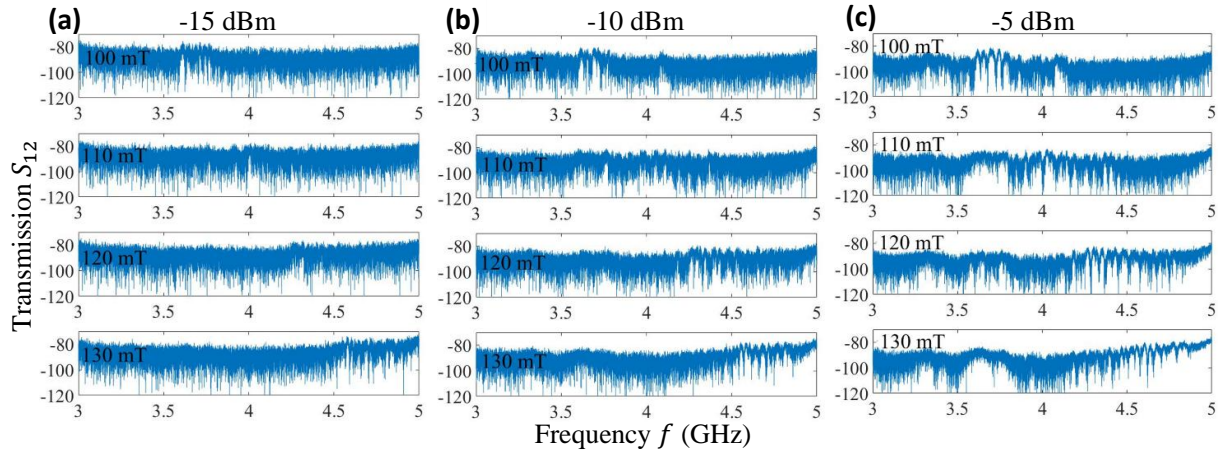


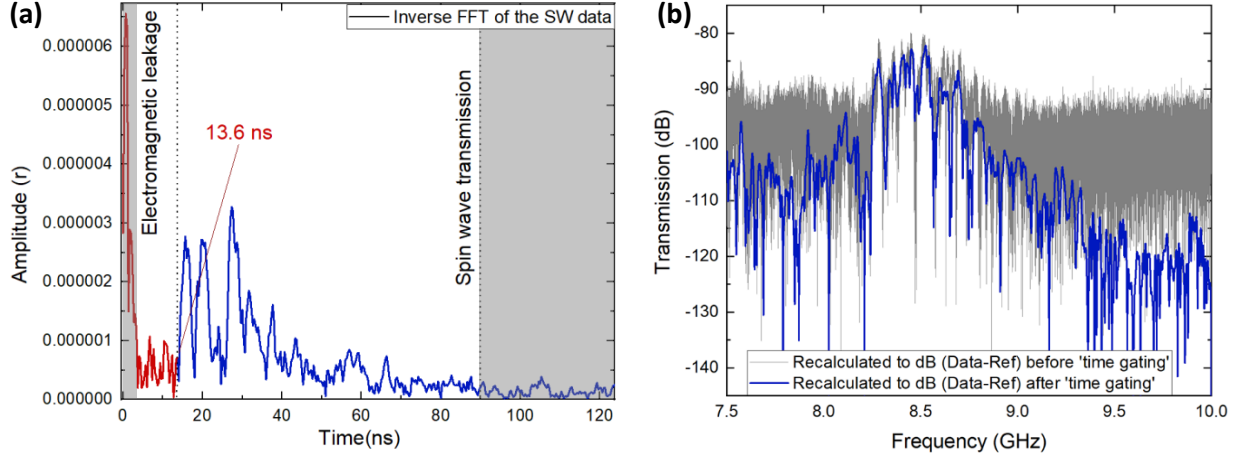
**Fig. S8:** Exemplary ‘time gating’ of the  $S_{12}$  spin-wave transmission at a bias field of  $\mu_0 H_{\text{ext}} = 260$  mT bias magnetic field: (a) Distinct peaks of spin-wave transmission and electromagnetic leakage in a time domain (inverse FFT from frequency domain); (b) Spin-wave transmission spectra (with a previously subtracted reference signal) before (gray) and after (blue) spurious signal removal. Time domain data in Fig. S3(a) converted back to frequency domain via FFT.

## 6. PSWS at different power levels

All PSWS measurement discussed in the main article were performed at microwave power of  $-10$  dBm. This value was identified as optimal based on a series of measurements at various VNA power levels, providing the best signal-to-noise ratio while maintaining operation within the linear regime (Fig. S9 (a)-(f) as indicated in the figures’ top caption). Measurements performed on a structure of interest in Damon-Eshbach configuration, with no averaging of the signal and the intermediate frequency bandwidth set to  $1$  kHz.



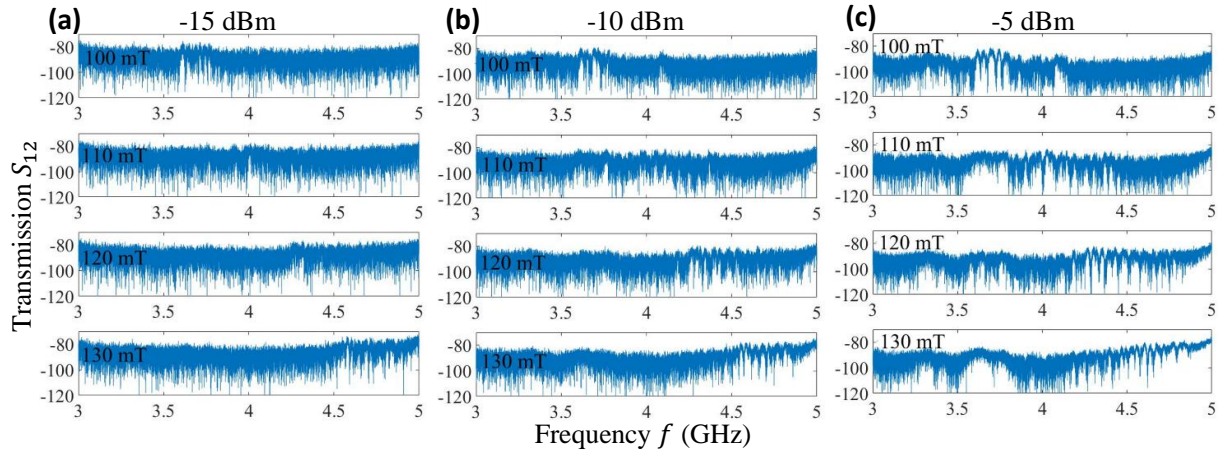
spin-wave velocity of  $\approx 340$  m/s (according to the TetraX simulations of the unstructured waveguide, *Section 3.3* of the Supplementary materials for the lowest fundamental volume mode  $n = 2$  slightly below  $3.1$  rad/ $\mu\text{m}$ ). This closely matches the second pulse found in the time-domain data, appearing at  $13.6$  ns. Therefore, a SW transmission window is further fixed to the time frame  $13.6$  ns –  $90$  ns, while setting the rest to zero, to eliminate the parasitic signal and noise. The obtained signal is then transformed back to the frequency domain via the FFT – Fig. S8(b). Note, that we do not differentiate here between the pure SW transmission and reflected components, e.g., triple transit.



**Fig. S8:** Exemplary ‘time gating’ of the  $S_{12}$  spin-wave transmission at a bias field of  $\mu_0 H_{\text{ext}} = 260$  mT bias magnetic field: (a) Distinct peaks of spin-wave transmission and electromagnetic leakage in a time domain (inverse FFT from frequency domain); (b) Spin-wave transmission spectra (with a previously subtracted reference signal) before (gray) and after (blue) spurious signal removal. Time domain data in Fig. S3(a) converted back to frequency domain via FFT.

## 6. PSWS at different power levels

All PSWS measurement discussed in the main article were performed at microwave power of  $-10$  dBm. This value was identified as optimal based on a series of measurements at various VNA power levels, providing the best signal-to-noise ratio while maintaining operation within the linear regime (Fig. S9 (a)-(f) as indicated in the figures’ top caption). Measurements performed on a structure of interest in Damon-Eshbach configuration, with no averaging of the signal and the intermediate frequency bandwidth set to  $1$  kHz.



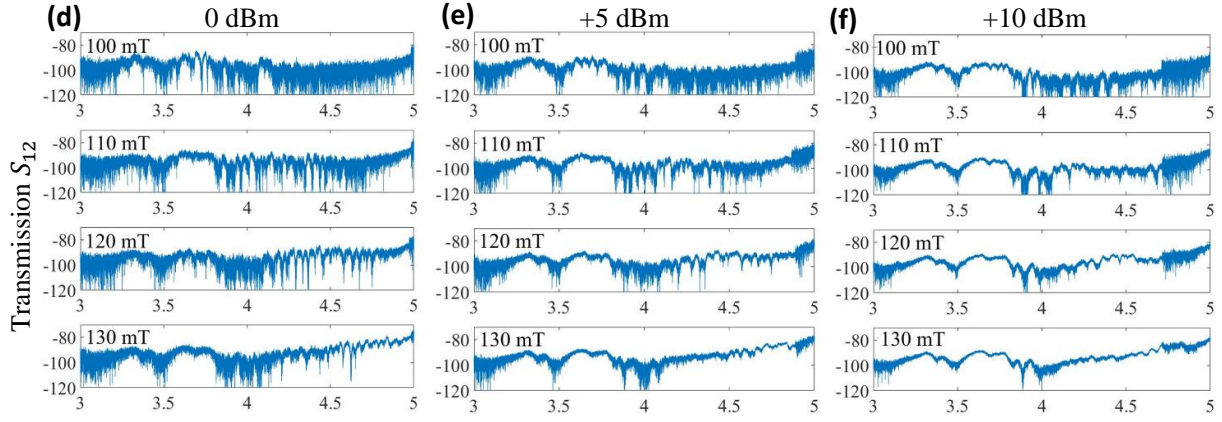
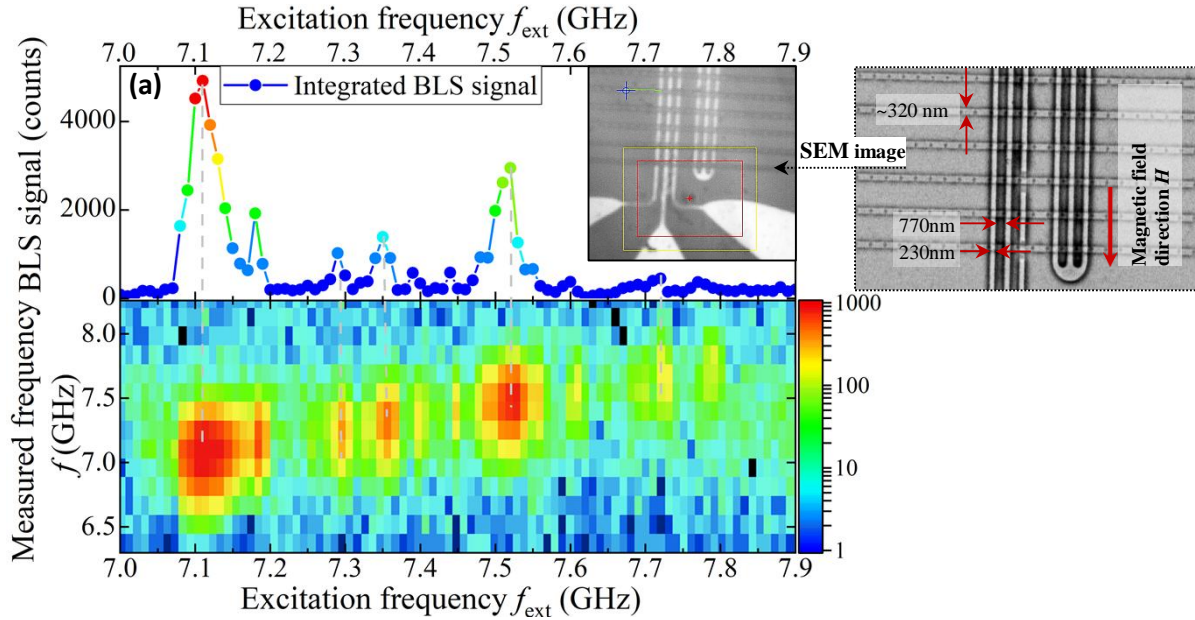


**Fig. S9:** Six  $S_{12}$  transmission spectra of a structure of interest at six different microwave power levels each for four different external magnetic fields, as indicated in the figures.

## 7. $\mu$ -BLS frequency sweep

To study the spin-wave transmission in a single magnonic crystal, we have performed series of microfocused Brillouin light scattering spectroscopy ( $\mu$ -BLS) measurements.  $\mu$ -BLS is a crucial technique for current investigation as it provides spatially resolved spin-wave mapping of magnetization dynamics at the submicron scale, with a smallest distinguishable feature  $\approx 300$  nm. High resolution is achieved at a loss of  $k$ -resolution, as light is collected from multiple angles, leading to a mixture of different  $k$ -components in the detected signal. This is unlike  $k$ -resolved BLS, which uses a collimated laser beam at a defined angle of incidence to selectively probe certain wavevectors, but uses a large laser spot  $> 50$   $\mu$ m.

The measurements were performed on a different structure than the one used in PSWS analysis, as it was accidentally damaged. However, all relevant geometrical parameters remained the same (i.e., average waveguide's width and the holes' size), just the holes position were more centered. Distance between the antennas was  $\approx 2$   $\mu$ m and number of conduits on antennas – 50, which were irrelevant for the BLS measurements.



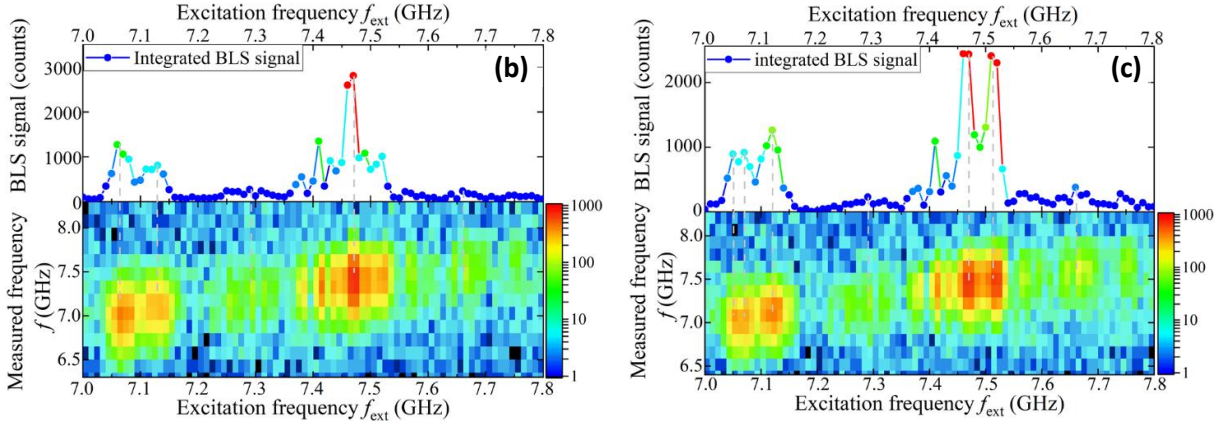


**Fig. S10:** BLS signal (detector counts) of the propagating spin wave as a function of a coherent excitation  $f_{\text{ext}}$  (x-axis) in a form of: **(top section of each figure)** 2D graph, where each y-axis point corresponds to the integrated measured frequency  $f$  over each respective excitation frequency  $f_{\text{ext}}$ ; **(bottom section of each figure)** 3D intensity map (log scale), where the y-axis shows the full range of measured frequency  $f$  at each excitation frequency  $f_{\text{ext}}$ , and BLS signal intensity is color-coded at z-axis. Three separate measurements (a) – (c) were performed at slightly shifted laser focus position along the short waveguide axis.

Firstly, we have performed the excitation frequency  $f_{\text{ext}}$  sweep of a single magnonic crystal conduit at a fixed distance of  $\approx 5 \mu\text{m}$  from coplanar waveguide, as shown at the set-up microscope's photo (Fig. S10(a), inset) and schematically at the SEM image of the investigated structure (Fig. S10(a) right panel). The BLS laser was positioned in the middle of the MC waveguide. However, as the waveguide's dimensions are at the resolution limit of the microscope, three measurements (Fig. S10(a) – (c)) were performed with the same input parameters, but with the laser focus slightly shifted. It is clearly seen how the spin-wave propagation path from the excitation antenna to the detecting laser position is moderately changed, with passband frequency peaks displaying similar periodic pattern, but differ in their amplitude. Also, the spin-wave spectra shown in Fig. S10(b) and (c) are slightly downshifted in frequencies, as each measurement was taken separately with laser position set every time anew.

The first passband peak appears around 7.05 GHz – 7.12 GHz with subsequent peaks spaced 0.19 GHz from each other (red-green areas on 3D maps). Regions dominated by the background BLS counts (blue areas on the 3D map) represent five band gaps measured 4.5 structural periods from the excitation antenna within a single MC waveguide. In patterned magnetic structures, inhomogeneous demagnetizing fields form at the edges of holes, locally modifying the internal magnetic field and leading to the localization of spin waves. These confined modes are highly sensitive to structural parameters such as hole size, spacing, and film thickness. As a result, fabrication imperfections—common in nanostructured thin films—can lead to variations in these parameters, contributing to the emergence of multiple peaks within one passband region, as well as changes to peaks' amplitude. Additionally, the generally lower signal intensity of propagating spin waves in thin films enhances the visibility of such parasitic modes.

Afterwards, we investigated the spin-wave transmission in the passband and band-gap regions by sweeping the laser position from 0 to 5  $\mu\text{m}$  away from the antenna in around 100 nm step. Note, that Fig. S11 demonstrates the maximum BLS intensity at the passband excitation frequency  $f_{\text{ext}} = 7.04 \text{ GHz}$  (red circles) and at the band-gap frequency  $f_{\text{ext}} = 7.2 \text{ GHz}$  (blue squares), not integrated as in Fig. S10, for more clear representation. The passband signal is an order of magnitude stronger than that of a bandgap, confirming the SW filtering. Linear fitting reveals a smaller slope for the bandgap signal (light-blue dots) compared to the passband (orange dashes), indicating suboptimal excitation efficiency due to coarse excitation frequency choice, shifted starting position of the linescan from the vicinity of the antenna and enhanced signal dissipation due to holes directly beneath the antenna.

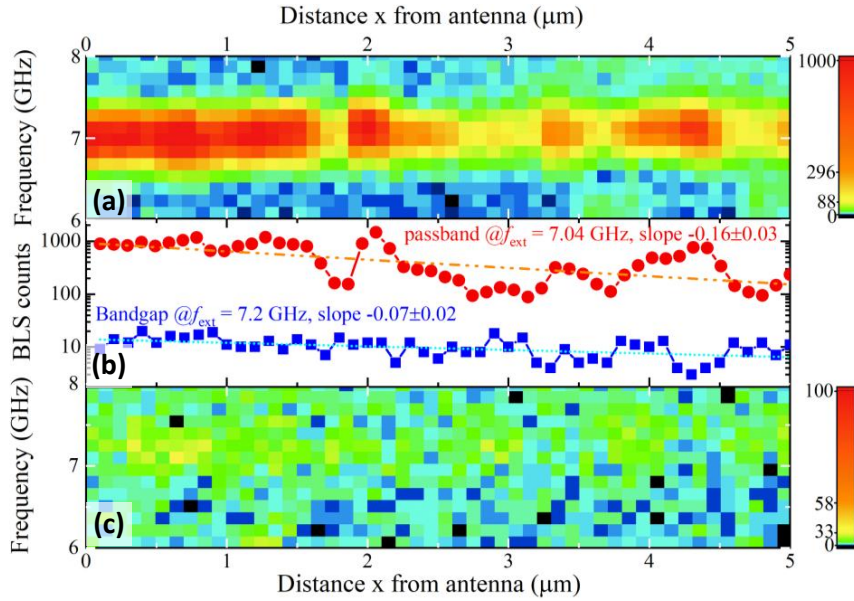


**Fig. S11:** BLS signal intensity of the propagating spin wave as a function of laser scan position 0-5  $\mu\text{m}$  from the antenna (x-axis) in a form of: a 3D intensity map, where the y-axis shows the measured frequency  $f$  at a passband (a) or band-gap (c) excitation frequencies  $f_{\text{ext}}$ , while the BLS signal intensity is color-coded on the z-axis; a 2D graph (b), where each y-axis point corresponds to maximum BLS counts at the respective passband and band-gap frequencies.

#### SUPPLEMENTARY MATERIALS LITERATURE:

- [S1] H. Merbouche, et al., "Frequency Filtering with a Magnonic Crystal Based on Nanometer-Thick Yttrium Iron Garnet Films" *ACS Appl. Nano Mat.*, **4**(1), 121–128 (2021). DOI: [10.1021/acsanm.0c02382](https://doi.org/10.1021/acsanm.0c02382)
- [S2] S. Manton, et al., "Reconfigurable spin wave modes in a Heusler magnonic crystal" *J. Appl. Phys.* **135**(5), 053902 (2024). DOI: [10.1063/5.0189486](https://doi.org/10.1063/5.0189486).
- [S3] N. Kanazawa, et al., "The role of Snell's law for a magnonic majority gate" *Sci. Rep.* **7**, 7898 (2017). DOI: [10.1038/s41598-017-08114-7](https://doi.org/10.1038/s41598-017-08114-7).
- [S4] V. Vlaminc and M. Bailleul "Spin-wave transduction at the submicrometer scale: Experiment and modeling" *Phys. Rev. B* **81**, 014425 (2010). DOI: [10.1103/PhysRevB.81.014425](https://doi.org/10.1103/PhysRevB.81.014425).
- [S5] B. A. Kalinikos, et al., "The dipole-exchange spin wave spectrum for anisotropic ferromagnetic films with mixed exchange boundary conditions" *J. Phys.: Condens. Matter* **2**, 9861 (1990). DOI: [10.1088/0953-8984/2/49/012](https://doi.org/10.1088/0953-8984/2/49/012).
- [S6] B. A. Kalinikos, and A. N. Slavin. "Theory of dipole-exchange spin wave spectrum for ferromagnetic films with mixed exchange boundary conditions" *Journal of Physics C: Solid State Physics* **19**(35), 7013 (1986). DOI: [10.1088/0022-3719/19/35/014](https://doi.org/10.1088/0022-3719/19/35/014).
- [S7] C. Heeg "Spin mechanics at radio frequencies" Ph.D. diploma thesis, Technische Universität München (2010).
- [S8] I. Zdru, F. Ciubotaru, C. Nastase, A. Florescu, A. A. Hamadeh, M. Geilen, A. Nicoloiu, G. Boldeiu, D. Vasilache, S. Iordanescu, et al., "Interaction of Acoustic Waves With Spin Waves Using a GHz Operating GaN/Si SAW Device With a Ni/NiFeSi Layer Between Its IDTs" *IEEE Transac. Ultras. Ferroelectr. Freq. Contr.* **72**(1), 30 (2025). DOI: [10.1109/TUFFC.2024.3463731](https://doi.org/10.1109/TUFFC.2024.3463731).